Numerical simulation of a capillary helium and helium-oxygen atmospheric pressure plasma jet: propagation dynamics and interaction with dielectric

C Lazarou[1,2], C Anastassiou[2], I Topala[3], A S Chiper[3], I Mihaila[4], V Pohoata[3] and G E Georghiou[1,2]

[1]*FOSS Research Centre for Sustainable Energy, Department of Electrical and Computer Engineering, University of Cyprus, Nicosia, 1678, Cyprus*
[2]*ENAL Electromagnetics and Novel Applications Lab, Department of Electrical and Computer Engineering, University of Cyprus, Nicosia, 1678, Cyprus*
[3]*Iasi Plasma Advanced Research Center (IPARC), Faculty of Physics, Alexandru Ioan Cuza University of Iasi, Iasi 700506, Romania*
[4]*Integrated Center of Environmental Science Studies in the North-Eastern Development Region (CERNESIM), Alexandru Ioan Cuza University of Iasi, Iasi 700506, Romania*

Corresponding authors: lazarou.constantinos@ucy.ac.cy, alina.chiper@uaic.ro and ionut.topala@uaic.ro

Abstract

Atmospheric pressure plasma jet (APPJ) can be generated in capillary tubes flowing with pure helium and with admixtures of oxygen into the pure helium. The jet exiting the tube can be used for a variety of applications through surface interaction. In this study, a two-dimensional axi-symmetric model has been developed to provide insight into the evolution of capillary helium plasma jet with and without the presence of oxygen admixtures and its interaction with a dielectric surface placed normal to the jet axis. The model considers the gas mixing of helium and ambient air and the analytical chemistry between helium, nitrogen and oxygen species. Experiments were performed in similar conditions as the simulations in order to get qualitative agreement between them. The numerical and experimental results show that the evolution of the helium plasma jet is highly affected by the introduction of oxygen admixtures. In particular, it was observed that the addition of oxygen admixtures in the helium gas promotes plasma bullet propagation on the axis of symmetry of the tube (instead off axis propagation for the pure helium plasma jet). On the other hand, the presence of the dielectric surface (the slab placed in front of the tube exit) forces the plasma bullet to spread radially. Furthermore, the plasma bullet speed decreases when the helium plasma jet is operated in the presence of oxygen admixtures. The numerical results also showed that He/O_2 plasma jets induced much higher electric fields on the dielectric surface in comparison to the pure helium plasma jet.

1. Introduction

Atmospheric pressure plasma jets are very promising for applications in the area of material science and biomedicine [1–8]. The advantage of the APPJ compared to other atmospheric pressure plasma devices is their ability to deliver in remote locations a wide range of reactive species, charge species, high electric fields and UV photons. Among APPJ devices, helium plasma jets with small amounts of nitrogen or oxygen admixtures, show very encouraging results for the above applications [9,10].

In the last two decades, significant efforts have been made for the understanding of the fundamental processes behind the operation of the APPJ devices. Particularly, Teschke et al. [11] and Lu and Laroussi [12] showed for the first time that plasma jet is not continuous as seen by the naked eye, but it consists of plasma bullets travelling at high speeds of the order of ~10

- 100 km/sec. Furthermore, it was observed that the plasma bullet has a ring shape and propagates in the channel formed by the helium in the air [13,14]. The importance of Penning reactions (PR) behind the ring structure of the plasma bullet has been indicated by many studies [15–18], as they observed the disappearance of this ring structure when admixtures were introduced into the helium gas. From [19], it was also observed that there is a minimum threshold for the helium mole fraction in the helium jet for the successful propagation of the plasma bullet. Recently many important experimental studies have been carried out providing very good insight into the characterization and understanding of these devices, the electric fields [20–25] and the different produced species [26–31]. However, in order to increase the understanding behind the operation of APPJ and to overcome some of the practical experimental limitations, numerical modelling has been increasingly used to simulate APPJ devices.

In the literature, there are remarkable simulation studies investigating the evolution of helium plasma jet devices providing insight into the fundamental processes during the discharge [32–45]. The numerical simulation studies indicate that the plasma bullet has the characteristics of an ionizing wave (streamer) [32–34,36,38]. The ring structure of the plasma bullet has been successfully captured in many numerical simulation studies [35,36,38,39,45]. Brenden et al. [36] showed the importance of helium-air channel for the successful propagation of the ionizing wave. Naidis [37] showed that increasing the applied voltage and the helium flow rate increases the propagation speed of the ionizing wave as well as the propagation length. On the other hand, increasing the tube radius for the same flow rate results in the decrease of the propagation length. Boeuf et al. [38] showed that by increasing the voltage pulse amplitude or rise time or preionization density the plasma bullet speed increases. In the same study, decreasing the tube radius shows an increase of the electron density on the plasma bullet head. The effect of air admixtures on the evolution of a helium plasma jet has been investigated by Naidis [40]. It was observed that the ring structure of a helium plasma jet disappeared when air admixtures were introduced into the helium gas due to the smoothing of the radial uniformity of plasma parameters inside the streamer channel. The effect of nitrogen impurities on the dynamic evolution of a helium plasma gun setup was investigated by Bourdon et al. [41]. It was shown that two and three body penning reactions are crucial for the discharge dynamics. It was also found that higher amplitudes of the applied voltage cause an increase of the ionization front velocity, confirming the results from Naidis et al. [32] and Boeuf et al. [38]. However, the ionization front velocity at different level of nitrogen admixtures in the helium gas was shown to be dependent on a complex coupling between the kinetics of the discharge, the photoionization and the 2D structure of the discharge in the tube. Norberg et al. [42] investigated the production of reactive oxygen and nitrogen species (RONS) for a He/O$_2$ plasma jet. It was shown that high flow rates and low repetition frequency results in the production of RONS that flow outside the tube. Furthermore, a higher applied voltage results in a higher production rate of RONS. Logothetis et al. [43] investigated the interaction of helium plasma jet with air. A flow alteration was observed when plasma was activated due to an induced electro hydrodynamic force acting on the fluid. Recently Lietz et al. [44] discussed processes in the He/air gas phase that heat up the gas and may cause the disturbance of the helium-air channel.

However, for practical applications, the importance of plasma jet lies on the interaction with surfaces (such as plastics, metals, biological tissue, liquids). Due to that, in the last few years emphasis is placed on numerical simulation studies of the plasma surface interaction [46–50]. Norberg et al. [46] investigated the interaction of a He/O$_2$ plasma jet with different surfaces (dielectrics with relative permittivity in the range of 2-80 and metal), and how plasma dynamics

and components are affected by this interaction. It was observed that as the relative permittivity increases, the speed of the ionizing wave increases as well as the density of plasma species. The metal surface presents similar features as the high permittivity surfaces (a conductive channel between the surface and the tube) but with negligible propagation of the ionizing wave along the metal. On the other hand, dielectrics with lower permittivity show a higher penetration of the electric field into the dielectric and a greater propagation of the ionizing wave along them. Similar observation has been made by Wang et al. [48], for a helium plasma jet impinging into dielectrics with different relative permittivity. Yan and Economou [49] investigated a helium plasma jet in ambient oxygen impinging on metal and dielectric surface. A conductive channel was observed to be developed between the plasma jet device and the metal surface without surface ionizing waves (SIW), while for the case of a dielectric surface SIW was developed similar to the one reported by Norberg et al. [46] and Wang et al. [48].

In this work, for the first time to our knowledge, the effect of oxygen admixtures on the evolution and interaction of a capillary helium plasma jet device with a dielectric surface is investigated numerically and observed experimentally. Several components such as secondary emission flux of electrons (SEFE), Penning reactions, and oxygen admixtures are all considered and integrated into the numerical model. Valuable insight is gained into the device by utilizing this detailed numerical model. For example the model gives an explanation as to why the helium plasma jet has a torus/ring like shape and it also explains why the addition of oxygen admixtures causes the plasma bullet to change to a sphere like shape. Furthermore, the model shows how a low level of oxygen impurities increases the induced electric field (IEF) on the dielectric surface, which is very important for biomedical applications of helium plasma jets.The use of capillary tubes for plasma generation [2,51], as is done in this study, is gaining attention for biomedical applications. Capillaries are small and flexible and generate low volume plasma streams that can be delivered to previously inaccessible anatomical structures. Furthermore, it has been observed that a small amount of oxygen admixtures into the helium increases the effectiveness of APPJ against cancer cells [9,10]. Since the plasma bullet mainly determines the interaction of the plasma jet with the surface, it is important to understand how the bullet and its interaction is affected by the introduction of O_2 into the helium gas. This study will mainly focus on: the evolution of He plasma jet, the effect of O_2 admixtures and the dielectric on the evolution and shape of plasma bullet, and the intensity of the induced electric field (IEF) on the dielectric surface for pure helium and with oxygen admixtures plasma jet. Furthermore, the effects of Penning reactions and the SEFE attributed to each ion in the mixture are also investigated through the same numerical model.

The paper is organised as follows. The experimental setup is described in section 2 and the simulation model with its boundary conditions in section 3 and input parameters to the simulation model in section 4. In section 5 the experimental results are presented, while in section 6 the simulation results. Finally, the conclusions are given in section 7.

2. Experimental Setup

The experimental setup is shown in Figure 1. A high-voltage (HV) electrode made of a copper band is wrapped on a 20 cm long capillary soda lime glass tube (VWR International) with internal diameter (ID) of 0.9 mm and outer diameter (OD) of 1.35 mm. The HV electrode is 1 cm in length and is placed ~ 1.5 mm away from the exit of the tube. A dielectric barrier made of fussed quartz vitreosil 077 (UQG Optics LTD) of 1 mm thickness, is placed in front of the capillary tube, close to the HV electrode. The gas-gap thickness is fixed at 2 mm, in this study. The working gas (He or He+O_2) is continuously injected through the capillary tube. The flow of helium (4.6 spectral purity, Linde) and oxygen (4.5 spectral purity, Linde) is

independently controlled using mass flow controllers (MKS 1179A coupled with MKS type 247 four channel readout). The total gas flow rate is 1 slm.

High-voltage monopolar pulses are delivered from a high-voltage pulse amplifier (Trek, Inc., model PD07016) driven by an arbitrary waveform generator (Tektronix, model AFG3022C). Square positive voltage pulses with amplitude of 4.0 kV, duration of 50 μs, rise time of 7.3 μs and frequency of 10 kHz are used to excite the discharge.

In order to capture the dynamic behaviour of the plasma jet, an Intensified Charged Coupled Device (ICCD) consisting of a high resolution (1344 x 1024 pixels) CCD camera (Hamamatsu, model C8484-05G) and an image intensifier unit (Hamamatsu, model C9546-03) with an overall spectral response of 330-880 nm is used. The ICCD camera gate (~ 40 ns) was synchronized with the discharge current pulse. Additionally, an adjustable delay was used to follow the temporal evolution of the discharge current pulse. Each image was automatically stored using 1 s integration time and smoothed using a moving average filter. The temporal resolution is given by the camera gate (40 ns) and the time interval between two consecutive pictures taken along the current pulse (10 ns around current maximum and 40 ns the rest), while the spatial resolution is given by the CCD array and its objective magnification. Our experimental arrangement allows us to take pictures of the discharge gap width (2 mm) with high spatial resolution of about 8 μm.
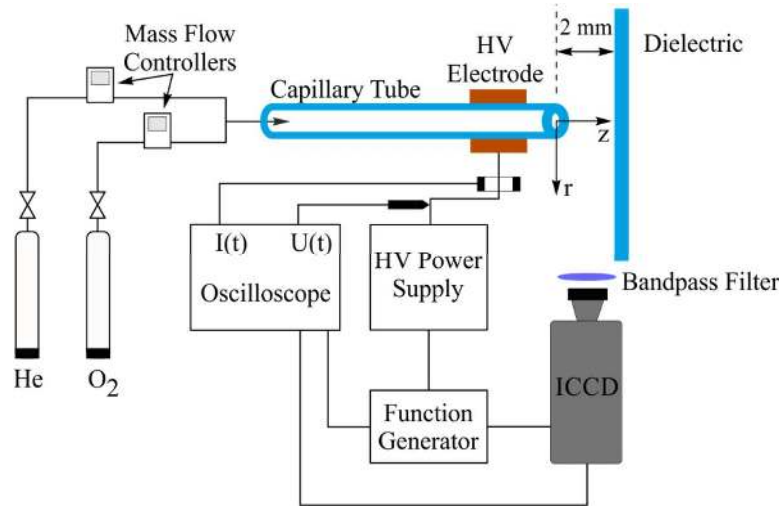

Figure 1. Experimental arrangement.

3. Model

For the simulation of the helium plasma jet a two-dimensional axi-symmetric model is used. The simulation procedure is divided into two parts. In the first part the mixing of the helium jet and the ambient air, where the air is treated as a single species, is evaluated through a gas dynamic model [52]. Due to the much slower speed of the fluid (~ 50 m/s) compared to that of the plasma bullet (~ 10^4 m/s), the gas dynamic model is solved in steady state. The calculated profiles of the air mole fraction and the mass average velocity are then fed into the second part of the simulation dealing with the time dependent plasma evolution [53]. It is noted that the gas dynamic model is solved only one time (before the plasma fluid model) and the air mole fraction is fed to the plasma fluid model as initial condition for the N_2 (79% of air) and O_2 (21% of air) species. Furthermore, for the initial concentrations of N_2 and O_2 an extra 40 ppm of air is added in the helium channel (79% and 21% of 40 ppm respectively), due to the air impurities in the helium bottle (99.996% purity). This procedure is followed by many published studies

4

[36,39,48,50] and it assumes that for the time scales of interest these species can be considered to be in local equilibrium. The simulation domain, material properties and dimensions are presented in Figure 2. The gas dynamic model is solved in the region ADML, while the plasma fluid model in the region HENO. At the flow rate of interest of 1 *l/min*, the Reynold's number, $R_e \sim 190$ and therefore the flow is laminar. For laminar flow the necessary length for the velocity profile to be fully developed in the tube is given by $0.05 \cdot Diameter \cdot R_e \approx 8.6\ mm$ [54]. Therefore, the additional length of 10 mm in the simulation domain for the gas dynamic model is sufficient for the helium gas velocity profile to be fully developed. In order to save simulation time and to focus on the plasma interaction with the dielectric surface, the plasma fluid model is solved in a smaller domain.
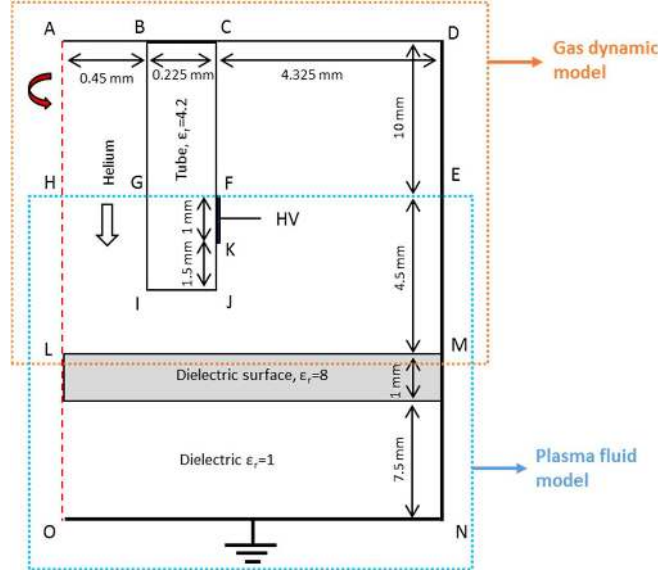

Figure 2: Axi-symmetric simulation domain for the gas and the plasma fluid model.

3.1 Gas dynamic model

The gas dynamic model describes the flow of the helium jet in the ambient air. In this model only two species are considered, helium and air. The helium-air mixing is obtained from solving the steady-state multi-component mass transport equation, without considering the chemical reaction term. This equation is appropriate when the species concentrations in the mixture are of the same order of magnitude and none of the species acts as a solvent. On the other hand, the mass average velocity of the mixture is obtained from solving the steady-state equations of the conservation of total mass and momentum. As an approximation, the heating of the gas is not considered (from the solution of the energy conservation equation), since it has been observed that it does not affect significantly the structure of the flow [55].

The multi-component mass transport equation is given below:

$$\nabla \cdot \left(\rho D_i^M \nabla \omega_i + \rho \omega_i D_i^M (\nabla M / M) \right) + \rho (u \cdot \nabla) \omega_i = 0, \ \ i = 1, \dots, Q - 1 \tag{1}$$

where ρ is the mixture gas density, D_i^M the mixture average diffusivity of species i, ω_i the mass fraction of species i, M the molar mass of the mixture, u the mass average velocity of the mixture and Q is the number of species in the mixture. For a binary system, as in this case, the multicomponent mass transport equation reduces to one equation. Equation (1) is solved only for the helium species and the air mass fraction is calculated from the equation:

5

$$\omega_{Air} = 1 - \omega_{He} \tag{2}$$

Due to the low gas speeds with a Mach number < 0.2 the gases can be considered incompressible and the density of the mixture can be computed from the species composition and gas temperature [55]. The mass average velocity field of the mixture is calculated from the equations of the conservation of total mass and momentum:

$$\nabla \cdot (\rho u) = 0 \tag{3}$$

$$\rho(u \cdot \nabla)u = \nabla \cdot (\mathrm{pI} + \mu(\nabla u + (\nabla u)^T) - 2/3\,\mu(\nabla \cdot u)\mathrm{I}) + F \tag{4}$$

where p is the pressure, I the unit matrix, μ the dynamic viscosity of the mixture and F is the body force field. The dynamic viscosity is calculated from Wilke's formula [56]. The body force field is considered as the buoyancy force exerted in helium gas due to the mixing of the gases:

$$F = g(\rho - \rho_{Air}) \tag{5}$$

where g is the gravity constant.

3.2 Boundary conditions of the gas dynamic model

The boundary conditions considered for all the equations presented in section 3.1 are summarized in Table 1. Particularly, the multi-component mass transport equation deals only with helium species. The flux of helium species (N_i) from the solid surfaces is considered to be zero:

$$-\vec{n} \cdot N_i = 0$$

$$N_i = \rho D_i^M \nabla \omega_i + \rho \omega_i D_i^M (\nabla M/M) + \rho(u \cdot \nabla)\omega_i \tag{6}$$

where $\vec{n}$ is the normal vector pointing towards the solid surface. The helium mass fraction is set to 1 at the entrance point of the tube nozzle, while the helium mass fraction is set to zero at boundaries located away from the tube. Regarding equations 3 and 4 describing the mass average velocity field, the following boundary condition is used for points away from the tube:

$$(-\mathrm{pI} + \mu(\nabla u + (\nabla u)^T) - 2/3\,\mu(\nabla \cdot u)\mathrm{I})\vec{n} = -p_0\vec{n} \tag{7}$$

where $p_0 = 1$ atm. This condition takes into account the normal stress but not the tangential one (it assumes the boundary is so far that there is no tangential flow). At the entrance point of the tube nozzle, the uniform axial velocity (u_0) is calculated from the helium flow rate in the tube to be $u_0 = 26.2$ m s^{-1}. On the tube surface, the velocity is set to zero (no-slip condition) [57].

Table 1: Boundary conditions considered for the gas fluid model. The letters A–O correspond to the ones found in Figure 2.		
Boundary	ω_{He}	u
AB	1	$-u_0\vec{n}$
BG, GI, IJ, JK, KF, FC, LM	Equation 6	0
CD, DE, EM	0	Equation 7

6

3.3 Plasma fluid model

The plasma fluid model describes the plasma evolution. This model has been thoroughly described in [53]. In summary, the model uses the continuity equation in the drift diffusion approximation for the description of electrons and electron energy, and the multi-component diffusion equation for the description of the heavy species in the mixture (neutral, excited and ion species). These equations are coupled with the Poisson equation for the description of the electric field. The continuity equations for the electrons and electron energy are:

$$\frac{\partial n_e}{\partial t} + \nabla \cdot \vec{\Gamma}_e = S_e - (u \cdot \nabla) n_e \tag{8}$$

$$\frac{\partial n_\varepsilon}{\partial t} + \nabla \cdot \vec{\Gamma}_\varepsilon = -e\vec{\Gamma}_e \cdot \vec{E} + S_\varepsilon - (u \cdot \nabla) n_\varepsilon \tag{9}$$

where n_e and n_ε are the electron and electron energy density respectively, $\vec{\Gamma}_e$ and $\vec{\Gamma}_\varepsilon$ represent the flux of electrons and electron energy respectively, $\vec{E}$ is the electric field, S_e is the source term for the production-destruction of electrons, S_ε is the source term that accounts for the energy gain or loss in elastic and inelastic collisions of electrons with the heavy species in the mixture and u is the mass average velocity of the mixture (calculated from the gas fluid model and used as input in this model). The heavy species in the mixture is calculated from the multi-component equation:

$$\rho \frac{\partial}{\partial t} (\omega_i) + \rho (u \cdot \nabla) \omega_i = \nabla \cdot \vec{j}_i + S_i, \quad i = 1, \dots, Q - 1 \tag{10}$$

where ρ is the density of the mixture, ω_i the mass fraction of species i, $\vec{j}_i$ the diffusive flux vector, S_i the source term and Q is the number of heavy species in the mixture. The density of the background gas (helium) is calculated from:

$$\omega = 1 - \sum_{i=1}^{Q-1} \omega_i \tag{11}$$

The electric field is calculated from the solution of Poisson's equation:

$$-\nabla \cdot \vec{D} = \rho_v \tag{12}$$

where $\vec{D}$ is the electric displacement field and ρ_v is the local charge.

3.4 Boundary conditions of the plasma fluid model

The boundary conditions for the plasma fluid model are described in detail in [53] and are summarized in Table 2. The flux of electrons and electron energy on the solid surface are set as follows:

$$\vec{n} \cdot \vec{\Gamma}_e = \left(\frac{1}{2} v_{e,th} n_e - a n_e \mu_e \vec{E} \cdot \vec{n}\right) - \sum_{i=1}^{Q} \gamma_i N_A \vec{n} \cdot \vec{j}_i \tag{13}$$

$$\vec{n} \cdot \vec{\Gamma}_\varepsilon = \left(\frac{5}{6} v_{e,th} n_\varepsilon - a n_\varepsilon \mu_\varepsilon \vec{E} \cdot \vec{n}\right) - \sum_{i=1}^{Q} \gamma_i \varepsilon_k N_A \vec{n} \cdot \vec{j}_i \tag{14}$$

7

where $\vec{n}$ is the normal vector pointing towards the solid surface, $v_{e,th}$ the thermal velocity, μ_e and μ_ε are the electron and electron energy mobility respectively, γ_k is the secondary electron emission coefficient, ε_k is the mean initial energy of secondary electrons and N_A is the Avogadro constant. The constant a is defined as follows:

$$a = \begin{cases} 1 \ \left(sgn(q)\vec{E}\cdot\vec{n} > 0\right) \\ 0 \ \left(sgn(q)\vec{E}\cdot\vec{n} \le 0\right) \end{cases} \tag{15}$$

where q is the charge of the considered species. The flux of the heavy species in the mixture at the solid surfaces is given by the following equation:

$$\vec{n}\cdot\vec{J}_i = M_i R_{surf,i} + aM_i\omega_i\mu_{i,m}z_i\left(\vec{n}\cdot\vec{E}\right) \tag{16}$$

where M_i is the molar weight of species i, $R_{surf,i}$ the surface reaction rate, $\mu_{i,m}$ the mixture-averaged mobility and z_i is the charge number of species i. For the neutral species in the mixture, the second term on the right side of equation (16) is zero. The charging of the dielectric surfaces is taken into account by using the following equations:

$$\hat{n}\cdot\left(\vec{D}_1 - \vec{D}_2\right) = \rho_s \tag{17}$$

where $\vec{D}_1$ and $\vec{D}_2$ are the displacement electric field in the plasma and in the dielectric surface respectively, and ρ_s is the surface charge accumulation on the dielectric surface, which is calculated by solving the following ordinary differential equation:

$$\frac{\partial \rho_s}{\partial t} = \vec{n}\cdot\vec{J}_e + \vec{n}\cdot\vec{J}_i \tag{18}$$

where $\vec{J}_e$ and $\vec{J}_i$ are the electron and ion current densities on the wall respectively.

The equations presented in section 3.1 to 3.4 are solved on an Intel Xenon E5-2630 V2 2.6 kHz (with 12 core) server using the chemical reaction engineering module (for GDM) and the plasma module (for PFM) of the COMSOL multiphysics simulation package [58]. The models GDM and PFM have 303,940 and 169,947 elements respectively, with the smaller mesh size of 5 µm located in the region of the plasma jet evolution and the larger mesh size of 100 µm located away from the evolution of the plasma streamer. There are about 573,400 and 1,231,000 degrees of freedom for the GDM and the PFM respectively. The equations for the GDM and the PFM are discretized by the Galerkin finite element method using linear element shape functions, and the resulting system is solved using the direct solver PARDISO. For the time integration (PFM) the backward Euler method is used. Each simulation required 5-7 days to be performed.

Table 2: Boundary conditions considered for the plasma fluid model. The letters A–O correspond to the ones found in Figure 2.

Boundary	n_e	n_ε	n_i [a)]	D
GI, IJ, JK, LM	Equation 13	Equation 14	Equation 16	Equation 17
KF	Equation 13	Equation 14	Equation 16	Applied voltage
HG, FE	$-\vec{n}\cdot\vec{\Gamma}_e = 0$	$-\vec{n}\cdot\vec{\Gamma}_\varepsilon = 0$	$-\vec{n}\cdot\vec{J}_i = 0$	$-\vec{n}\cdot D = 0$
GF	---	---	---	$-\vec{n}\cdot D = 0$

EM	$-\vec{n} \cdot \vec{\Gamma}_e = 0$	$-\vec{n} \cdot \vec{\Gamma}_\varepsilon = 0$	$-\vec{n} \cdot \vec{j}_i = 0$	Ground
MN, NO	---	---	---	Ground
[a] Represents the heavy species in the mixture, such as the neutrals, excited and ion species				

4. Input parameters in the plasma fluid model

For the simulation of the plasma fluid model, 107 reaction channels (see Table 3 in Appendix A) and 14 species are considered. The species are electrons, He ground state atoms, He_m metastable species $He(2s^3S)$ and $He(2s^1S)$, He_2^m, He^+ and He_2^+ positive helium ions, N_2 ground state molecules, N_2^+ and N_4^+ positive nitrogen ions, O_2 ground state molecules, O_2^+ and O_4^+ positive oxygen ions, O^-, O_2^- negative oxygen ions. The excitation reactions for the production of N_2 at the vibrational states $(v = 1 - 4)$ and at the states of $N_2(A^3\Sigma_u^+ (v = 0 - 4))$, $N_2(A^3\Sigma_u^+ (v = 5 - 9))$, $N_2(A^3\Sigma_u^+ (v > 9))$, $N_2(B^3\Pi_g)$, $N_2(W^3\Delta_u)$, $N_2(B^3\Sigma_u^-)$, $N_2(a^1\Sigma_u^-)$, $N_2(a^1\Pi_g)$, $N_2(W^1\Delta_u)$, $N_2(C^3\Pi_u)$, $N_2(E^3\Sigma_g^+)$, $N_2(a^1\Sigma_g^+)$ are considered in the chemistry of the model in order to calculate the electron energy lost through these reactions. However, in order to save simulation time these species are not tracked separately in the model (they are all treated as N_2), similar to [48]. In the same way, the excitation of O_2 at the vibrational states $(v = 1 - 4)$ and at the states of $O_2(a^1\Delta_g)$ and $O_2(b^1\Sigma_g^+)$ are taken into account for the electron energy loss but in the simulation model they are all treated as O_2.

In Appendix A (Table 3), the rate coefficient of reactions 1-3, 24-38 and 52-60 are calculated from the solution of Boltzmann's equation with the two term approximation [59]. The procedure followed for these calculations is described in detail in our previous paper [53]. The above calculations also provide the transport parameters of the electrons and electron energy. The transport and rate coefficients are calculated only once and stored in tables as a function of the mean electron energy and air mole fraction. For these calculations, the air mole fraction was varied in the range of 10^{-5} to 1 (10 steps for every decade, i.e.$10^{-5}, 2 \cdot 10^{-5} ... 10^{-4}, 2 \cdot 10^{-4}, ... 1$). The interpolation between the different values of air mole fraction was linear. These coefficients are then retrieved from the tables during the operation of the plasma fluid model. The transport parameters for all the heavy species and their reaction with solid surfaces are the same as defined in [53]. As the surface charge accumulation on the dielectrics is not known, the secondary electron emission coefficient (seec) is considered as an adjustable parameter. For the positive ions in the mixture, the seec is set to 0.1 since that value gives good agreement between the experimental and numerical results. Furthermore, this value lies in the acceptable range as estimated experimentally [60]. The energy of the secondary electrons is set to 5 eV for the helium ions, and 3 eV for the nitrogen and oxygen ions. No secondary electrons are considered from other species in the mixture. Photoionization is not considered in this study, but instead a uniform background density of electrons and positive/negative ions is used, similar to other published works [39,48–50]. The density of the different species in the mixture is as follows: electrons are set to 10^{13} m^{-3}, heavy species (He_m, He_2^m, He_2^+, N_2^+, N_4^+, O_2^+, O_4^+, O^-, and O_2^-) are set to one order of magnitude lower than electrons i.e. 10^{12} m^{-3} (electroneutrality through the concentration of He^+ is hence satisfied), He^+ is set to a value that satisfies electroneutrality in the mixture, N_2 and O_2 are determined from the gas dynamic model (79% and 21% of air respectively) and He the background gas is calculated from equation 11. For the initial concentrations of N_2 and O_2 an extra 40 ppm of air is added in the helium channel (79% and 21% of 40 ppm respectively), due to the air impurities in the helium bottle (99.996% purity). Beyond the work shown in the manuscript we varied the initial densities of electrons and heavy species in the range of $10^8 – 10^{15}$ m^{-3} without noticeable changes in the results. The model uses the same voltage pulse waveform and parameters as the one applied experimentally.

5. Experimental results

For the experimental study, He and He+O_2 (1000 ppm) plasma jets are considered. The ICCD camera is used to capture the dynamic evolution of the plasma bullet presented in Figure 3. The results presented in Figure 3 correspond to the rise time of the positive applied voltage, more exactly to the positive discharge current. The time of 0 ns corresponds to the time the maximum emission intensity of the plasma bullet coincides with the tube exit (z=0 mm). From Figure 3a, for the pure helium plasma jet, it can be seen that the plasma bullet forms two symmetric lobes during its propagation. These lobes indicate a torus (ring) like shape for the plasma bullet. Similar experimental observations were also made in [13,14]. For this case, the radius of the torus remains almost constant up to 1 mm (half way between the tube exit and the dielectric surface), while after 1 mm the radius starts increasing until the plasma bullet hits the dielectric surface. On the other hand, when 1000 ppm of oxygen admixture is introduced in the helium gas, the plasma bullet appears disk like and centred on the axis of symmetry during its propagation from the tube towards the dielectric surface. This is true up to 1 mm from the tube exit, and indicates a sphere like shape for the plasma bullet. The change of plasma bullet shape, from torus like shape (He plasma jet) to sphere like shape (He+O_2 (1000 ppm)), was also observed in [15–18,40], when admixtures were introduced in the helium gas. For distances longer than 1 mm and as the plasma bullet starts approaching the dielectric, the disk shape starts splitting and moves away from the axis of symmetry forming a torus. The above observations can be summarized as: (a) the addition of oxygen admixtures in the helium gas promotes the plasma bullet propagation on the axis of symmetry of the tube; (b) the presence of the dielectric surface (the slab placed in front of the tube exit) forces the plasma bullet to spread radially. Furthermore, the addition of oxygen admixtures causes a reduction of the plasma bullet speed. For the interpretation of these experimental observations, the simulation results will be analysed, for both pure helium and with 500, 1000, 1500 and 2000 ppm of oxygen.
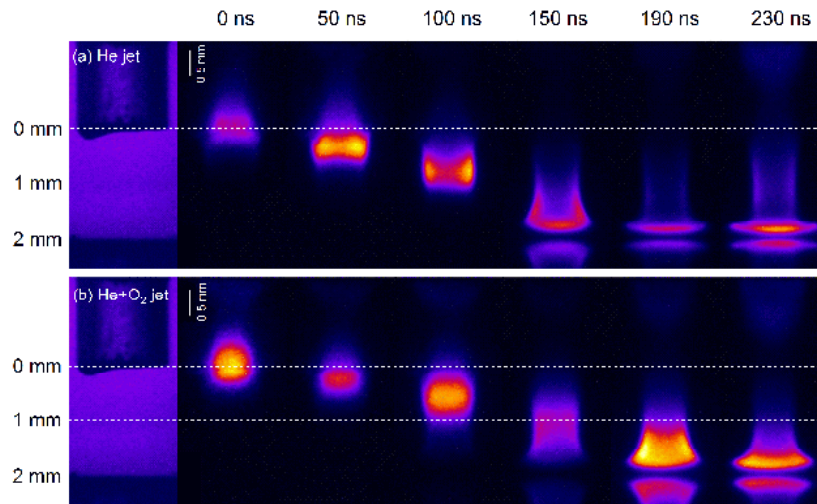

Figure 3: Spatio-temporal evolution of the plasma bullet for (a) He and (b) He+O_2 (1000 ppm) plasma jet. Time 0 ns corresponds to the plasma bullet just about the exit of the tube. The three dashed lines indicate the axial distance from the tube nozzle for z=0, 1 and 2 mm.

6. Analysis of the simulation results

In this section, the two-dimensional axi-symmetric plasma fluid model described in section 3 with the input parameters of section 4 is used to shed light into the experimental observations presented in section 5. It is noted that all the results presented in this section correspond to the rise time of the applied voltage. From the simulation results, it is observed that the evolution of the plasma jet has the characteristics of a streamer [14,38,61]. Consequently, in order to investigate its propagation, it is important to study the ionization rate on the streamer head. This will provide good insight into the evolution of the total light observed experimentally with the ICCD camera (presented in Figure 3) as it is expected to follow the propagation of the streamer. Furthermore, the interaction of the streamer with the dielectric surface and how it is affected by the introduction of oxygen admixtures is investigated in this section. In order to have comparisons with the experimental conditions the case of pure helium and with 1000 ppm admixtures of oxygen will be analysed in detail before the effects of different levels of oxygen (500-2000 ppm) are investigated. The simulation analysis will focus on the following:

- The reasons for the formation of torus shaped plasma bullet structure for the case of pure helium.
- The reasons for the change of plasma bullet structure to sphere shape once oxygen is added.
- The effect of the dielectric on the evolution of the plasma bullet.
- The effect of oxygen admixtures on the plasma bullet speed.
- The intensity of the induced electric field (IEF) on the dielectric surface for pure helium and with oxygen admixtures.

6.1 Evolution of the pure helium plasma jet

The helium-air mixture for the experimental setup presented in section 2 is obtained from the gas dynamic model and is shown in Figure 4. This shows that inside the tube prior to the exit, it is pure helium as expected. After it exits, it starts mixing with air, but it can be clearly seen that it forms a channel of almost pure helium that extends to the dielectric surface. The width of that channel is approximately the width of the tube. The mixing with air becomes more prevalent (the mole fraction of pure helium drops) away from the axis of symmetry ($r = 0$ mm) and as the gas propagation distance increases. This result is then fed into the plasma fluid model and the process is repeated for the case of adding 1000 ppm of oxygen to the helium gas (this is not shown here because it is indistinguishable from Figure 4).
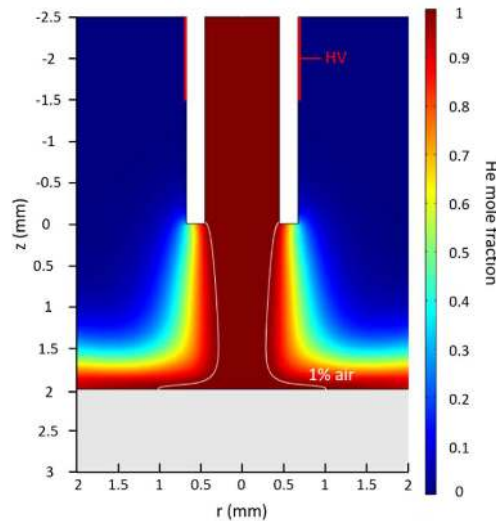

Figure 4: Helium-air mixture for the case of pure helium plasma jet obtained from the gas dynamic model. The white line shows the air at 1%.

For the analysis of the results, the evolution of the streamer is divided into three parts: first, propagation of the streamer from the tube towards the dielectric, second, interaction of the streamer with the dielectric surface, and third, propagation of the streamer along the dielectric surface. In the simulation model, the *streamer evolution is defined as the dynamic motion of the total ionization rate with the streamer head (plasma bullet) being the peak of that total ionization rate*. The terms streamer head, plasma bullet and peak of total ionization rate will be used interchangeably throughout this study. The streamer will be analysed for the positions and times illustrated in Figure 5. The time 0 ns is set to when the streamer head coincides with the tube exit (z=0 mm). Points 1-7 in Figure 5 correspond to the case when the streamer is moving towards the dielectric and point 8 to the case when it reaches the dielectric, while points 9-11 the propagation of the streamer in the r direction (after it hits the dielectric surface).

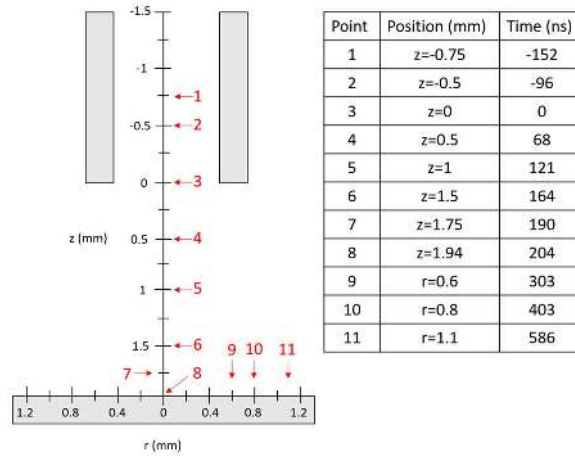| Point	Position (mm)	Time (ns)
1	z=-0.75	-152
2	z=-0.5	-96
3	z=0	0
4	z=0.5	68
5	z=1	121
6	z=1.5	164
7	z=1.75	190
8	z=1.94	204
9	r=0.6	303
10	r=0.8	403
11	r=1.1	586

Figure 5: Positions and corresponding times of the streamer head (total ionization rate) propagation for the He plasma jet. The time 0 ns corresponds to the streamer head coinciding with the tube exit (z=0 mm).

6.1.1 Spatio-temporal evolution of the streamer from the tube towards the dielectric

The spatio-temporal evolution of the total ionization rate is presented in Figure 6, for the same points defined in Figure 5. It is noted that the min and max values in Figure 6 are different for each sub figure, and therefore they are presented separately in each one. The applied voltage at time -152 ns (Figure 6a) is 1.85 kV and is considered the breakdown voltage, as it corresponds to the instance when the streamer starts to propagate. In particular, at this time the electric field created by the positive ions in the mixture becomes high enough to cause ionization and excitation hence propelling the streamer forward along the axis of symmetry towards the dielectric. The streamer shape changes during propagation. Initially the shape is disk like (Figure 6a) but by the time it exits the tube (Figure 6b and Figure 6c) it breaks into two lobes and then remains almost constant until it reaches 1 mm away from the dielectric (see Figure 6d and Figure 6e). From that point onwards its radius keeps increasing forming more distinct lobes (see Figure 6f and Figure 6g) until it hits (reaches) the dielectric, at which point its maximum is closer to the axis of symmetry (Figure 6h). The evolution of the streamer head (total ionization rate) presented below agrees qualitatively with the experimental results shown in Figure 3a.
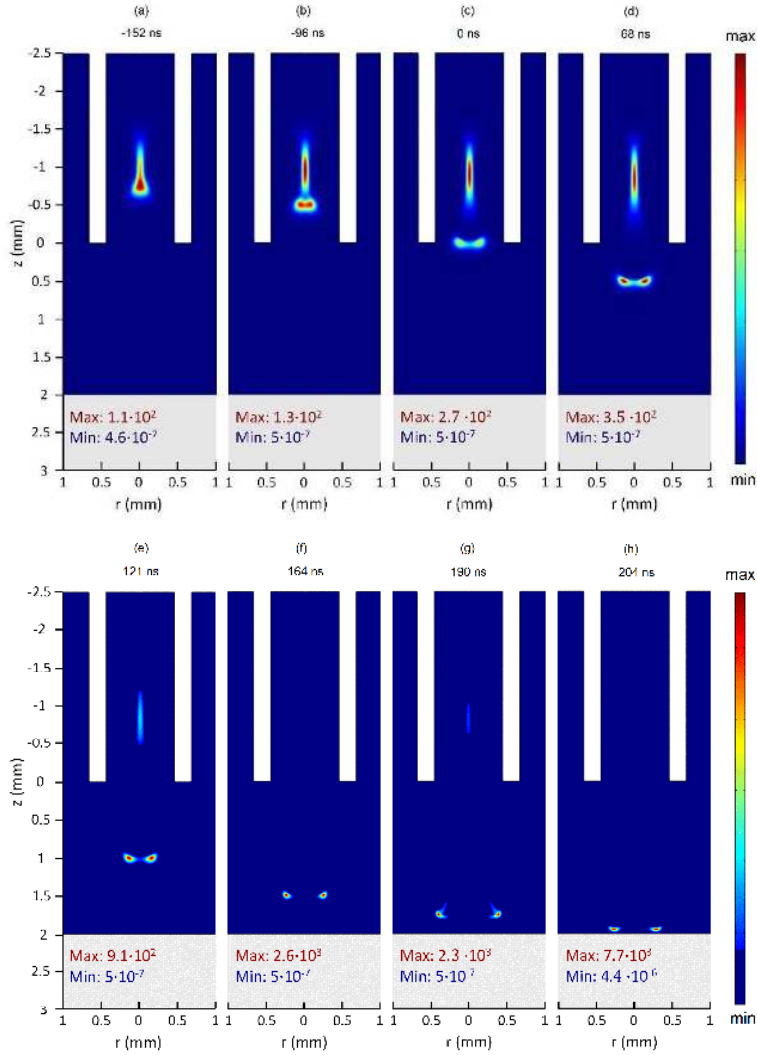
Figure 6: Simulation results of the spatio-temporal evolution of the total ionization rate (time snapshots as in Figure 5), for the He plasma jet. The total ionization rate has units of mol/m^{3}s.

6.1.2 *Electron production*

In order to understand the evolution of the plasma bullet, the electron production in front of the streamer head is further investigated. In Figure 7 the electron production rate is presented in logarithmic scale at -152 ns which corresponds to the same time snapshot of the total ionization rate shown in Figure 6a. Figure 7 shows the electron production being maximum at z=-0.75 mm which, as expected, coincides with the streamer head in Figure 6a. Away from the streamer head at z = 0.1 mm, the electron production pointed with arrows in Figure 7, shows that there is also a relatively high electron production at the boundary with air (r~0.35 mm).These electrons are mainly produced from the Penning reactions (PR) of the nitrogen and oxygen molecules by the He$_m$ species (R43, R51, R73 and R74, see Figure 19 in Appendix B). Those electrons will act as seeds accelerating into the tube and feeding the streamer head promoting the propagation of the streamer in the lateral direction creating a torus shape for the plasma bullet (see Figure 6b-Figure 6c). In order to ensure the validity of this conclusion, another simulation was performed (see Figure 20 in Appendix B), without considering Penning reactions in the kinetic scheme (i.e. their rate coefficients were set to zero) and the torus like

13

shape of the plasma bullet was not observed. In this case, the propagation of the plasma bullet occurs on the axis of symmetry of the tube and has a sphere like shape. The importance of Penning reactions on the evolution of helium DBD has been shown in several studies [41,62–68].
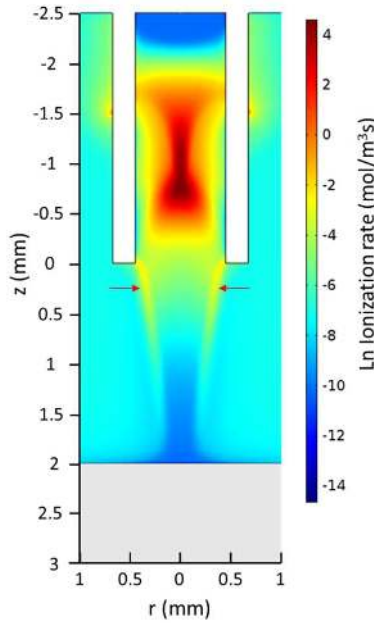

Figure 7: Simulation results of electron production rate in logarithmic scale for the He plasma jet at time -152 ns.

Once out of the tube and up to 1 mm away from the dielectric, the radius of the streamer remains almost constant, (see Figure 6d and Figure 6e). This is because the electron production in front of the streamer head presents peak at similar radius as the torus radius of the streamer (see Figure 21a in Appendix B). As can be seen, those electrons are mainly produced through Penning reactions of He_m with N_2 and O_2 molecules. After 1 mm from the tube exit, the torus radius of the streamer increases (see Figure 6f and Figure 6g) as the production of electrons in front of the streamer occurs at larger radius. Those electrons are mainly produced through Penning reactions of He_m and He_2^m with N_2 and O_2 molecules (see Figure 21b in Appendix B).

Close to the dielectric, the shape of the plasma bullet is affected by the electrons emitted from the dielectric surface. The SEFE attributed to each ion in the mixture when the streamer is far from the dielectric and when it approaches the dielectric surface (same time snapshots as Figure 6e and Figure 6g corresponding to streamer head at 1 and 1.75 mm respectively) are presented in Figure 8a and Figure 8b respectively. It is noted that SEFE corresponds to the last term on the right hand side of equation 13. As can be seen from Figure 8a, the SEFE is much higher on the sides (r~0.5 mm) than on the centre (r=0 mm). The major contributors to the SEFE are the O_4^+ ions that due to mixing with air are higher on the sides than in the centre. It is worth mentioning that the contribution of O_4^+ is dominant because most ions are eventually converted to O_4^+ (see schematic diagram of Figure 6 presented in [53]). However, as the streamer head approaches the dielectric surface (Figure 6g) the electric field in the region between streamer head and the dielectric surface increases, and that causes the positive ions to accelerate towards the dielectric surface. This increases the SEFE from all the ions and particularly from the helium ions as seen in Figure 8b. The SEFE due to the helium ions species is increased in the centre of the dielectric, eventually causing the decrease of the streamer head torus radius as seen in Figure 6h. It is noted that when seec is set to zero, the decrease of the

streamer torus radius when the plasma bullet reaches the dielectric surface is not observed (see Figure 22 in Appendix B).
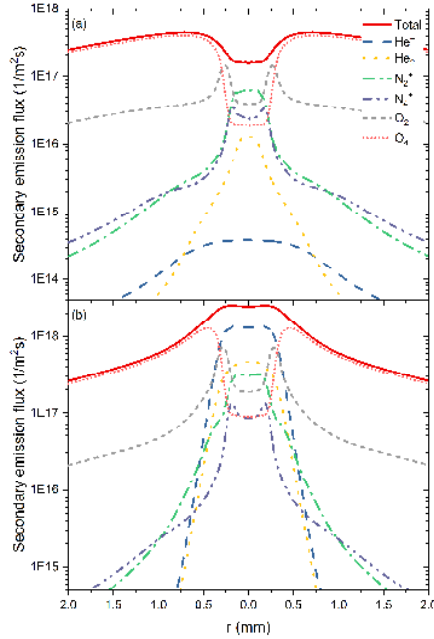

Figure 8: Simulation results of the secondary emission flux of electrons (SEFE) attributed to the different ions for the times (a) 121 ns and (b) 190 ns, for the He plasma jet.

6.1.3   Interaction of the streamer with the dielectric surface

As the streamer propagates towards the dielectric, it causes the accumulation of a surface charge. That surface charge induces an axial electric field that opposes and eventually negates the axial electric field of the streamer. That will stop the axial propagation of the streamer. Consequently, the radial electric field dominates, and the streamer starts propagating laterally (parallel to the dielectric). To illustrate that, the surface charge accumulation and the electric field in z and r direction along the dielectric surface are presented in Figure 9, at different times which correspond to the cases of before (121, 164 and 190 ns), during (204 ns) and after (303, 403 and 586 ns) the streamer head reaches the dielectric surface. The positions of streamer head for these times are indicated in Figure 5. As can be seen from Figure 9, as the plasma streamer approaches the dielectric surface, the electric fields (in z and r directions) on the dielectric surface start increasing. As the streamer head reaches the dielectric surface (204 ns), the electric field in z and r direction increase considerably leading to surface charge accumulation. The axial electric field, E_z, due to the interaction of the streamer with the dielectric surface is ~ 37 kV/cm. It is important to note that the axial electric field and the surface charge accumulation during the interaction of the streamer with the dielectric surface present their peaks off axis, indicating a torus-like interaction of the plasma streamer with the dielectric surface. After that time, the surface charge accumulation continues to build up causing the reduction in the axial electric field. After some time, the radial electric field dominates, and the streamer proceeds to propagate radially (parallel to the dielectric surface). The results shown in Figure 9 associated with the streamer propagation in the radial direction (times 303, 403 and 586 ns) are analysed below when this case is investigated.
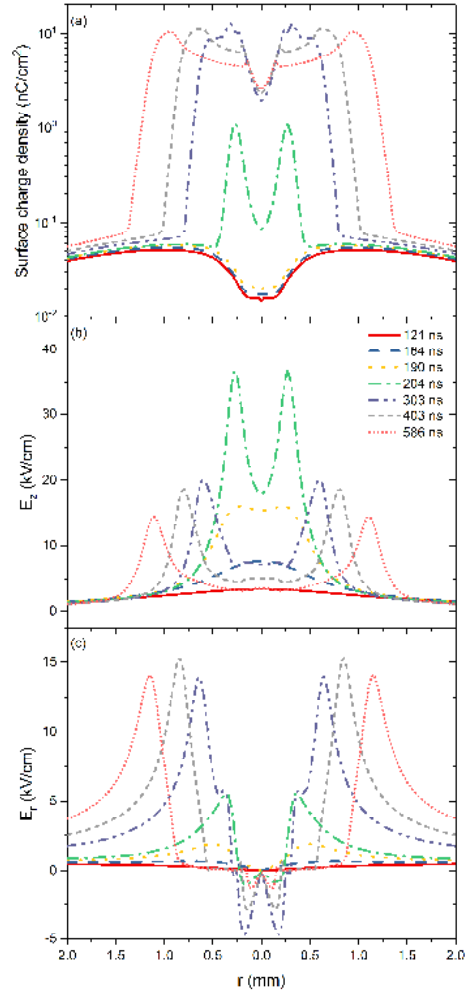
15

Figure 9: Simulation results of the (a) surface charge density, (b) electric field in z direction (axial) and (c) electric field in radial direction during the propagation of the streamer, for the He plasma jet.

6.1.4 *Spatio-temporal evolution of the streamer along the dielectric surface*

The spatio-temporal evolution of the total ionization rate during the propagation of the streamer along the dielectric surface is presented in Figure 10, for three different times (positions of the streamer head from the axis of symmetry of the tube: 0.6, 0.8 and 1.1 mm, see Figure 5). It is shown that when the streamer reaches the dielectric surface, it continues parallel to it at a height of ~ 60 - 70 µm charging the surface below it (see Figure 9a). This increases the surface charge eventually shielding the axial electric field behind the streamer head (see Figure 9b). However, the axial and radial electric fields decrease gradually (Figure 9b and Figure 9c), causing the reduction of the ionization rate on the streamer head (see Figure 10). This continual reduction of ionization rate will eventually stop the propagation of the streamer. From the simulation results, it has been found that during the plasma bullet propagation along the dielectric surface the electron concentration is about $5 \cdot 10^{18}$ [m^{-3}] while the mean electron energy reduces from 20 eV to 10 eV. These results, provide a Debye length in the range of 10 to 15 µm. The sheath thickness found here (60-70 µm), as expected, corresponds to a few times the Debye length, which is in agreement with previous studies [69].
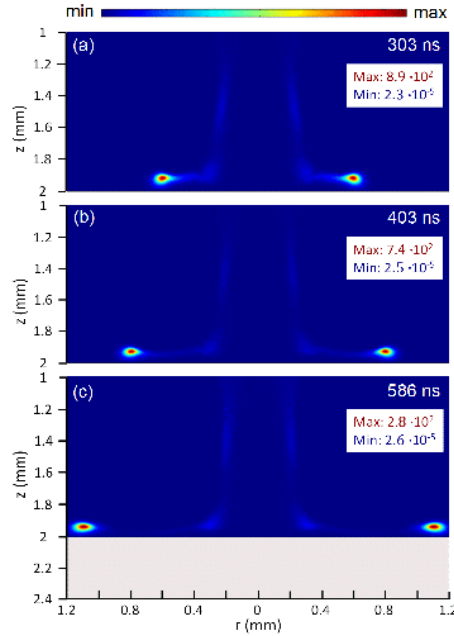
16

Figure 10: Simulation results of the spatio-temporal evolution of the total ionization rate along the dielectric surface (time snapshots as in Figure 5), for the He plasma jet. The total ionization rate has units of mol/m^{3}s.

6.2 Evolution of the He+O$_2$ (1000 ppm) plasma jet

Similar to the analysis for pure helium plasma jet, the present analysis is divided into three parts: evolution of the streamer from the tube towards the dielectric surface, interaction of the streamer with the dielectric surface and evolution of the streamer along the dielectric surface. The spatio-temporal evolution of the total ionization rate during the streamer propagation will be analysed for the positions and times illustrated in Figure 11.
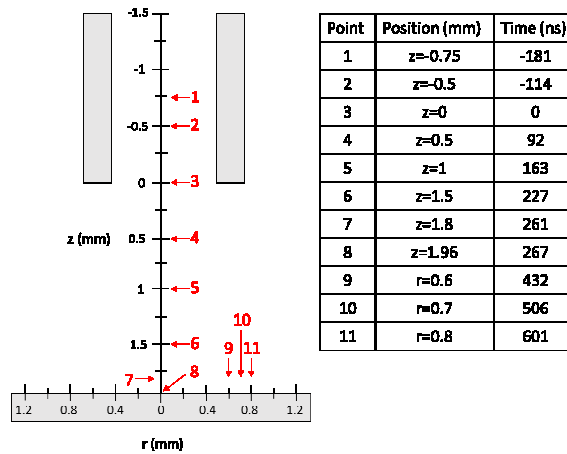

Point	Position (mm)	Time (ns)
1	z=-0.75	-181
2	z=-0.5	-114
3	z=0	0
4	z=0.5	92
5	z=1	163
6	z=1.5	227
7	z=1.8	261
8	z=1.96	267
9	r=0.6	432
10	r=0.7	506
11	r=0.8	601

Figure 11: Positions and corresponding times of the streamer head (total ionization rate) propagation for the He+O$_2$ (1000 ppm) plasma jet. The time 0 ns corresponds to the streamer head coinciding with the tube exit (z=0 mm).

6.2.1 Spatio-temporal evolution of the streamer from the tube toward the dielectric

The propagation of the streamer from the tube towards the dielectric surface for the He+O$_2$ (1000 ppm) plasma jet is analysed here. The total ionization rate is presented in Figure 12 for the same points as in Figure 11. As can be observed from Figure 12a, the total ionization rate

17

initially increases in the region close to the electrodes on the axis of symmetry of the tube and has a disk like-shape. At this time (-181 ns which corresponds to the instance when the streamer starts to propagate) the applied voltage is 1.23 kV (breakdown voltage). The decrease of the breakdown voltage once oxygen admixtures are introduced in a helium barrier discharge is explained in our previous study [53]. Particularly, in such discharges (helium with admixtures of air components), the ions in the mixture are mainly increased due to the increase of He^+ and He_m species (see Figure 6 in [53]). The increase of O_2 concentration in the mixture benefits the reactions associated with this species (such as Penning ionization reaction, charge transfer reaction etc.). As a result, a lower concentration of He_m and He^+ is required for ion production. The concentration of the former species is highly dependent on the electron temperature and consequently on the breakdown voltage. Then, in helium with admixtures of air components, the increase of air concentration results in a decrease of the breakdown voltage.

Once the streamer begins to move towards the dielectric surface, its propagation remains on the axis of symmetry up until 1 mm from the tube exit (Figure 12b-Figure 12e). After 1 mm from the tube exit, the streamer forms two symmetric lobes centred on the axis of symmetry (Figure 12f). However, as the streamer approaches the dielectric surface, its maximum approaches the axis of symmetry of the tube (see Figure 12g and Figure 12h). The streamer exhibits qualitatively similar behaviour to the experimental results presented in section 5 (see Figure 3b).
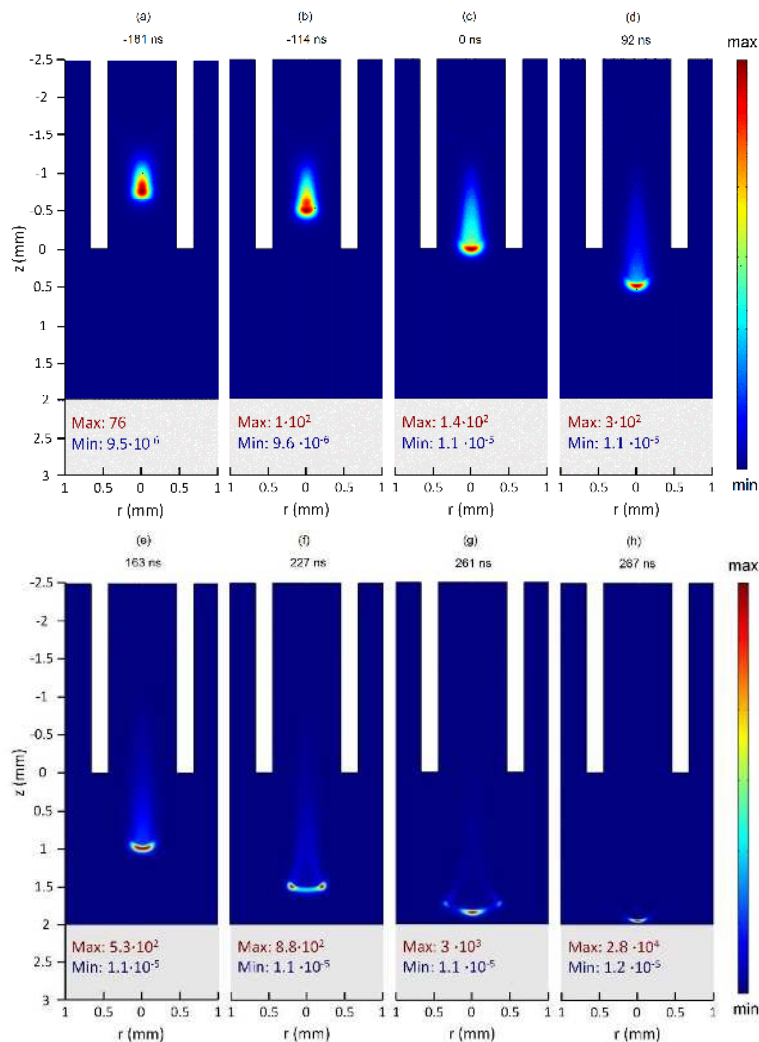
Figure 12: Simulation results of the spatio-temporal evolution of the total ionization rate (same time snapshots as in Figure 11), for He+O_2 (1000 ppm) plasma jet. The total ionization rate has units of mol/m^{3}s.

6.2.2 Electron production

In order to further understand the evolution of the plasma bullet, the electron production in front of the streamer head is investigated. In Figure 13 the electron production rate is presented in logarithmic scale at -181 ns which corresponds to the same time snapshot of the total ionization rate shown in Figure 12a. Figure 13 shows the electron production being maximum at z=-0.75 mm which, as expected, coincides with the streamer head in Figure 12a. However, unlike the case for pure helium there is no off axis (on the side) peak production of electrons outside the tube. Therefore, the streamer does not break to form a torus shape and remains disk like propagating on the axis of symmetry (see Figure 12a-Figure 12c).

Those electrons are mainly produced from the Penning ionization of the oxygen molecules by the He_m species (R73 and R74, see Figure 23 in the Appendix B) and due to the high amount of oxygen admixtures in the helium channel, are not affected much by the mixing with atmospheric air. As a result, the electron production around the centre (for r<0.35 mm) is almost constant and does not exhibit strong peaks on the edges (r~0.35 mm). This is in contrast to the pure helium plasma where the mixing with air plays an important role in the production of electrons.
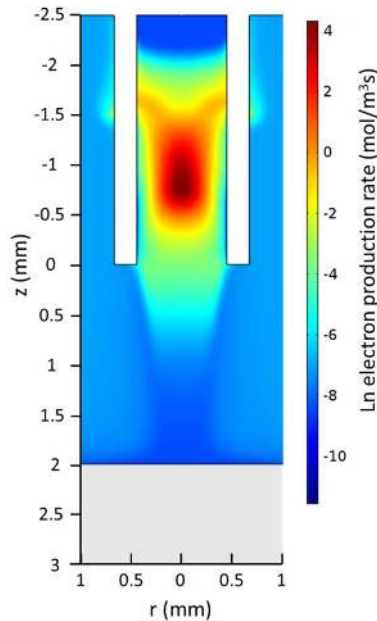

Figure 13: Simulation results of electron production rate in logarithmic scale for He+O_2 (1000 ppm) plasma jet at time – 181 ns.

Once out of the tube, the streamer continues to propagate on the axis of symmetry (see Figure 12d-Figure 12e), as electrons in front of the streamer are mainly produced in the helium channel. Those electrons are mainly produced from Penning reactions of He_m with O_2 (see Figure 24a in Appendix B). After 1 mm of the streamer from the tube exit, the maximum of electron production in front of the streamer head occurs off axis. Those electrons feed the streamer head from the sides, promoting its propagation in the lateral direction creating a torus shape for the plasma bullet (see Figure 12f). The off axis production of electrons is mainly due to the Penning reaction of He_m and He_2^m with nitrogen molecules (see Figure 24b in Appendix B). It is noted that when the Penning reactions are eliminated from the kinetic scheme (i.e. their

rate coefficients are set to zero) the torus like shape of the plasma bullet is no longer observed (see Figure 25 in Appendix B).

In order to investigate the effect of the dielectric on the plasma bullet shape, the SEFE attributed to each ion in the mixture when the streamer is far from the dielectric and when it approaches the dielectric surface (same time snapshot as Figure 12e and Figure 12g corresponding to streamer head at 1 and 1.8 mm respectively) are presented in Figure 14a and Figure 14b respectively. As can be seen from Figure 14a, the SEFE is much higher on the sides (r~0.5 mm) than in the centre (r=0 mm). However, as the streamer head continues approaching the dielectric surface, the SEFE peak is at the axis of symmetry (r = 0 mm) as shown in Figure 14b. This promotes the propagation of the streamer on the axis of symmetry of the tube making the shape more disk like again (shown in Figure 12g and Figure 12h). The major contributor to the SEFE close to the centre are the He^+ species. It is noted that when the seec is set to zero the approaching of the streamer on axis of symmetry is not observed (see Figure 26 in Appendix B).
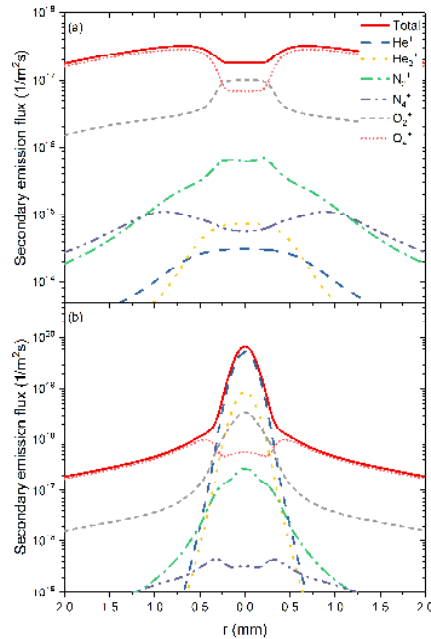

Figure 14: Simulation results of secondary emission flux of electrons (SEFE) attributed to the different ions for the times (a) 163 ns and (b) 261 ns, for He+O$_2$ (1000 ppm) plasma jet.

6.2.3 Interaction of the streamer with the dielectric surface

The interaction of the streamer head with the dielectric surface (Figure 12h), causes the accumulation of surface charge. That surface charge induces an axial electric field that opposes and eventually negates the axial electric field of the streamer. That will stop the axial propagation of the streamer. Consequently the radial electric field dominates and the streamer starts propagating laterally (parallel to the dielectric). To illustrate that, the surface charge density on the dielectric surface and the electric fields in z and r direction before, during and after the streamer reaches the dielectric surface are presented in Figure 15. The positions of streamer head for these times are indicated in Figure 11.

As can be seen from Figure 15, before the streamer reaches the dielectric surface (times = 163, 227 and 261 ns), the surface charge density and the electric field on the dielectric surface are low. Once the streamer reaches the dielectric (267 ns), they both increase. During the interaction of the streamer with the dielectric surface, the axial electric field reaches the value of ~51 kV/cm which is higher in comparison to the pure He plasma jet (~37 kV/cm). The

difference in the peak values of E is most likely caused by the higher concentration of electrons ~ $1.25 \cdot 10^{19}$ m^{-3} in the case of He/O$_2$ plasma jet in comparison to ~ $5 \cdot 10^{18}$ m^{-3} for the He plasma jet. Furthermore, the electric field in the He/O$_2$ plasma jet does not have torus-like shape as in the pure helium plasma jet case but presents its peak on the axis of symmetry. After the streamer reaches the dielectric surface, the charge density increases until it cancels the axial electric field of the streamer. The remaining radial electric field causes the streamer to continue to propagate parallel to the dielectric. The results shown in Figure 15 associated with the streamer propagation in the radial direction (times 432, 506 and 601 ns) are analysed below.
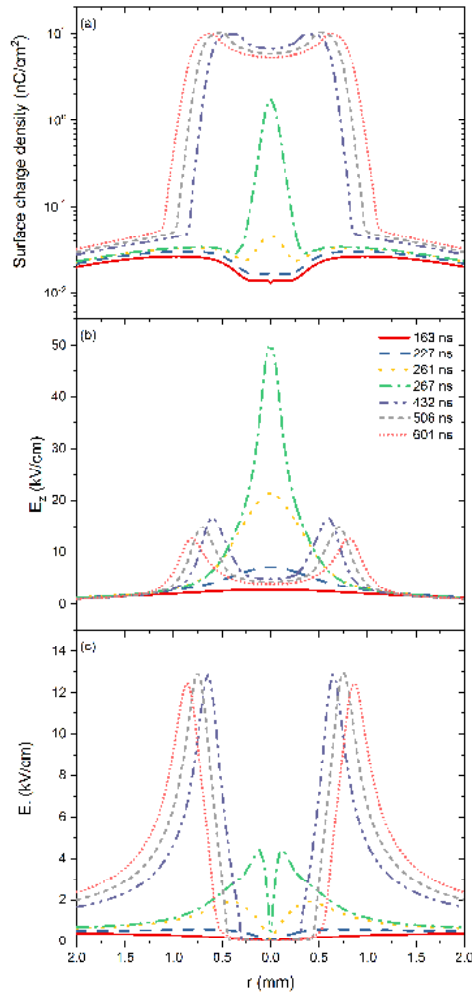

Figure 15: Simulation results of the (a) surface charge density, (b) electric field in z direction and (c) electric field in r direction during the propagation of the streamer for He+O$_2$ (1000ppm) plasma jet

6.2.4 Propagation of the streamer along the dielectric surface

The spatio-temporal evolution of the total ionization rate during the propagation of the streamer along the dielectric surface is presented in Figure 16, for three different positions of the streamer head from the axis of symmetry of the tube (0.6, 0.7 and 0.8 mm). After the streamer reaches the dielectric surface, its propagation continues along the dielectric surface at a height about 60 - 70 μm above it. During the propagation of the streamer head, positive ions are accelerated towards the dielectric surface (charging the dielectric surface, see Figure 15a) causing the eventual shielding of the electric field behind streamer head (see Figure 15b).

Furthermore, as can be observed from Figure 15b and Figure 15c, the axial and radial electric fields decrease gradually, causing the reduction of the ionization rate on the streamer head (see Figure 16). This continual reduction of ionization rate will eventually stop the propagation of the streamer.
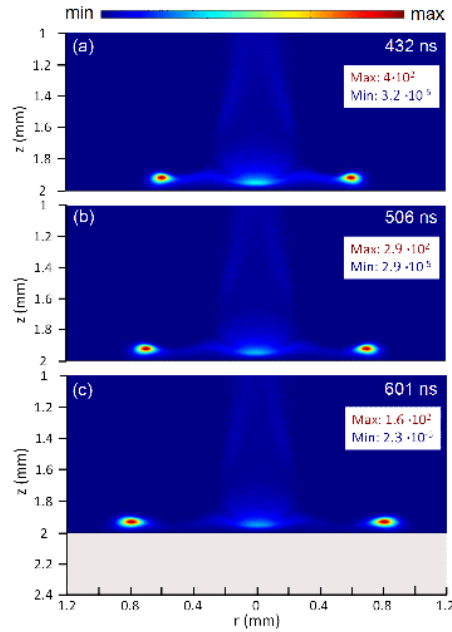

Figure 16: Simulation results of time snapshots of the total ionization rate of He+O_2 (1000 ppm) plasma jet, during the propagation of the streamer along the dielectric surface. The total ionization rate has units of mol/m^{3}s.

6.3 *Effects of different level of oxygen admixtures on the plasma evolution and interaction with the dielectric surface*

As oxygen admixtures vary from 500-2000 ppm the general behaviour of the streamer and its interaction with the dielectric surface does not change significantly, and therefore the detailed analysis presented in section 6.1 and 6.2 will not be repeated here. Two important parameters such as the streamer speed and IEF (during the interaction of the streamer with the dielectric surface) are presented here. The propagation speed of the streamer, derived from Figure 17, shows a significant difference between pure helium and He+O_2, albeit little variation with different admixture levels. The average speed is 7.7 km/s and 6.1 km/s for pure helium and He+O_2 plasma jet respectively. This reduction of the speed of the plasma bullet when 1000 ppm of oxygen admixtures is introduced in the helium gas is also observed experimentally (see section 5).
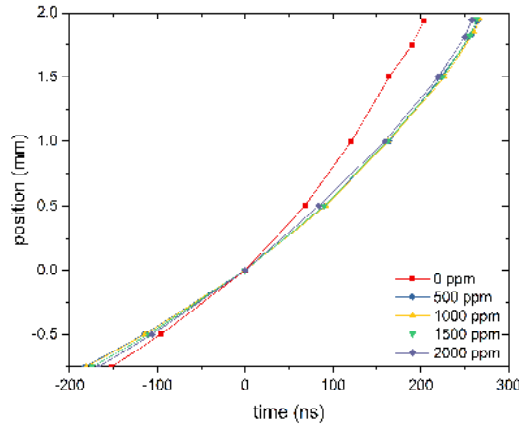
Figure 17: Simulation results of the axial position of the streamer head as a function of time.

The IEF built on the dielectric surface (during the streamer surface interaction) at different levels of oxygen admixtures in the helium gas is presented in Figure 18. The results presented correspond to the times of 204, 265, 267, 264 and 258 ns for the case of 0, 500, 1000, 1500 and 2000 ppm of oxygen admixtures in the helium gas. As can be observed, for the case of He+O_2 plasma jet there is a time delay for the interaction of the plasma jet with the surface. Furthermore, the He+O_2 plasma jet generates higher IEF in comparison to the pure helium plasma jet. Furthermore, the peak of the IEF on the dielectric surface is on the axis of symmetry for He+O_2 plasma jets and off the axis of symmetry for pure helium plasma jet. The maximum IEF (~ 55 kV/cm) occurs for the case of 1500 ppm of oxygen admixtures in the helium gas. Even though this will be the subject of future studies, it is worth mentioning that the higher electric fields for He+O_2 plasma jets could have significant implications for biomedical applications. They could make cells more susceptible to electroporation and could account for the observation that the presence of oxygen impurities in the Helium plasma jet can increase cancer cell apoptosis [9,10].
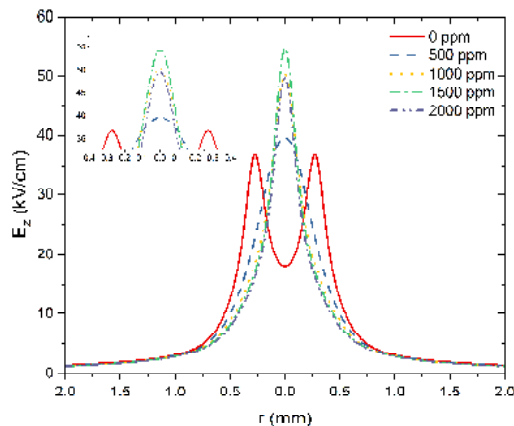

Figure 18: Induced electric field on the dielectric surface at different level of oxygen admixtures.

7. **Conclusions**

In this study, a two dimensional model was used to shed light into the evolution of a capillary helium plasma jet with and without the presence of oxygen admixtures and its interaction with a dielectric surface. The level of oxygen admixtures considered in this study is in the range of 500 to 2000 ppm. The simulation results show that oxygen admixtures highly

23

affect the streamer shape, propagation speed, and the induced electric field on the dielectric surface. The shape of the plasma bullet during its propagation is controlled by the generation of seed electrons in front of the streamer head. For $He+O_2$ plasma jet, the shape of the bullet remains sphere like for propagation up to 1 mm away from the dielectric. This is because the seed electrons are mainly produced uniformly along the axis of symmetry in the helium channel. They are produced through Penning ionization of helium metastable species with the admixture of O_2 molecules. After 1 mm from the tube exit, the streamer forms two symmetric lobes centred on the axis of symmetry due to the off axis production of electrons in front of the streamer head. Those electrons are mainly produced through Penning reactions of He_m and He_2^m with N_2 molecules. In the case of pure helium jet the bullet will be torus shape because seed electrons in the helium channel are mainly generated on the edges of the channel through Penning ionization of nitrogen and oxygen molecules by He_m and He_2^m species (due to the higher N_2 and O_2 in this region from atmospheric air mixing). It should be noted that for both cases, once the streamer head gets very close to the dielectric (~ 0.1 - 0.2 mm) it is pulled towards the centre (the axis of symmetry) due to the high generation of SEFE on the axis of symmetry. Furthermore, it was observed that the plasma bullet speed decreases when the helium plasma jet is operated in the presence of oxygen admixtures. Finally, one of the most significant results is the observation of much higher induced electric field on the dielectric surface with the introduction of the optimal amount of oxygen admixtures. This is very important, since in some applications where the APPJ is to be used to destroy (or cause the apoptosis of) diseased cells, higher electric fields mean higher electroporation of the cells and consequently higher amounts of reactive species or even therapeutic drugs successfully introduced into the cells.

Acknowledgments

Appendix A.

Table 3: Rate coefficients for helium, nitrogen and oxygen reactions.

Reaction No.	Reaction equation[a]	Rate constant[b]	Threshold (eV)	Ref
1	$e^- + He \rightarrow e^- + He$	$f(\varepsilon, n)$	0	[70]
2	$e^- + He \rightarrow e^- + He_m$	$f(\varepsilon, n)$	19.82	[70]
3	$e^- + He \rightarrow 2e^- + He^+$	$f(\varepsilon, n)$	24.58	[70]
4	$e^- + He_m \rightarrow 2e^- + He^+$	$2.254 \times 10^{-13} T_e^{-0.1241} e^{-5.725/T_e}$	4.78	[71]
5	$e^- + He_m \rightarrow e^- + He$	2.9×10^{-15}	-19.82	[72,73]
6	$e^- + He_2^m \rightarrow e^- + 2He$	3.8×10^{-15}	-17.9	[72]
7	$2e^- + He^+ \rightarrow e^- + He_m$	$7.8 \times 10^{-50}(T_e/T_g)^{-4.4}$	-4.78	[74]
8	$2e^- + He_2^+ \rightarrow He_m + He + e^-$	2.8×10^{-32}	0	[72]
9	$e^- + He + He_2^+ \rightarrow He_m + 2He$	3.5×10^{-39}	0	[72]
10	$2e^- + He_2^+ \rightarrow He_2^m + e^-$	1.2×10^{-33}	0	[72]
11	$e^- + He + He_2^+ \rightarrow He_2^m + He$	1.5×10^{-39}	0	[72]
12	$He_m + He_m \rightarrow He_2^+ + e^-$	$2.03 \times 10^{-15}(T_g/300)^{0.5}$	-18.2	[75]
13	$He_m + He_m \rightarrow He^+ + He + e^-$	$8.7 \times 10^{-16}(T_g/300)^{0.5}$	-15.8	[75]
14	$He^+ + 2He \rightarrow He_2^+ + He$	$1.4 \times 10^{-43}(T_g/300)^{-0.6}$	0	[75]
15	$He_m + 2He \rightarrow He_2^m + He$	2×10^{-46}	0	[75]
16	$He_m + He_2^m \rightarrow He^+ + 2He + e^-$	$5 \times 10^{-16}(T_g/300)^{0.5}$	-13.5	[72]
17	$He_m + He_2^m \rightarrow He_2^+ + He + e^-$	$2 \times 10^{-15}(T_g/300)^{0.5}$	-15.9	[72]
18	$He_2^m + He_2^m \rightarrow He^+ + 3He + e^-$	$3 \times 10^{-16}(T_g/300)^{0.5}$	-11.3	[72]
19	$He_2^m + He_2^m \rightarrow He_2^+ + 2He + e^-$	$1.2 \times 10^{-15}(T_g/300)^{0.5}$	-13.7	[72]
20	$e^- + He^+ \rightarrow He_m$	$6.76 \times 10^{-19} T_e^{-0.5}$	0	[76]
21	$e^- + He + He^+ \rightarrow He_m + He$	$7.4 \times 10^{-47}(T_e/T_g)^{-2}$	0	[74]
22	$e^- + He_2^+ \rightarrow He + He_m$	$7.12 \times 10^{-21}(T_e/T_g)^{-1.5}$	0	[77]
23	$e^- + He_2^m \rightarrow He_2^+ + 2e^-$	$9.75 \times 10^{-16} T_e^{0.71} e^{-3.4/T_e}$	3.4	[75]
24	$e^- + N_2 \rightarrow e^- + N_2$	$f(\varepsilon, n)$	0	[78]
25	$e^- + N_2 \rightarrow e^- + N_2 \, (v = 1 \, to \, 4)$	$f(\varepsilon, n)$	0.3, 0.6, 0.9, 1.1	[78]
26	$e^- + N_2 \rightarrow e^- + N_2\left(A^3\Sigma_u^+ \, (v = 0 - 4)\right)$	$f(\varepsilon, n)$	6.2	[78]
27	$e^- + N_2 \rightarrow e^- + N_2\left(A^3\Sigma_u^+ \, (v = 5 - 9)\right)$	$f(\varepsilon, n)$	7	[78]
28	$e^- + N_2 \rightarrow e^- + N_2\left(B^3\Pi_g\right)$	$f(\varepsilon, n)$	7.4	[78]
29	$e^- + N_2 \rightarrow e^- + N_2(W^3\Delta_u)$	$f(\varepsilon, n)$	7.4	[78]
30	$e^- + N_2 \rightarrow e^- + N_2\left(A^3\Sigma_u^+ \, (v > 9)\right)$	$f(\varepsilon, n)$	7.8	[78]
31	$e^- + N_2 \rightarrow e^- + N_2\left(B^3\Sigma_u^-\right)$	$f(\varepsilon, n)$	8.2	[78]
32	$e^- + N_2 \rightarrow e^- + N_2(a^1\Sigma_u^-)$	$f(\varepsilon, n)$	8.4	[78]
33	$e^- + N_2 \rightarrow e^- + N_2(a^1\Pi_g)$	$f(\varepsilon, n)$	8.6	[78]
34	$e^- + N_2 \rightarrow e^- + N_2(W^1\Delta_u)$	$f(\varepsilon, n)$	8.9	[78]
35	$e^- + N_2 \rightarrow e^- + N_2(C^3\Pi_u)$	$f(\varepsilon, n)$	11	[78]
36	$e^- + N_2 \rightarrow e^- + N_2\left(E^3\Sigma_g^+\right)$	$f(\varepsilon, n)$	11.9	[78]
37	$e^- + N_2 \rightarrow e^- + N_2(a^1\Sigma_g^+)$	$f(\varepsilon, n)$	12.3	[78]
38	$e^- + N_2 \rightarrow 2e^- + N_2^+$	$f(\varepsilon, n)$	15.5	[78]
39	$e^- + N_4^+ \rightarrow 2N_2$	3×10^{-13}	0	[79]
40	$2e^- + N_4^+ \rightarrow 2N_2 + e^-$	3.17×10^{-42}	0	[71]
41	$2e^- + N_2^+ \rightarrow e^- + N_2$	3.17×10^{-42}	0	[80]

42	$e^- + N_2^+ \rightarrow 2N$	$2.36 \times 10^{-14}(T_e)^{-0.5}$	0	[80]
43	$He_m + N_2 \rightarrow e^- + N_2^+ + He$	5×10^{-17}	0	[71]
44	$He_2^m + N_2 \rightarrow e^- + N_2^+ + 2He$	5×10^{-17}	0	[71]
45	$He^+ + N_2 \rightarrow N_2^+ + He$	6.5×10^{-16}	0	[81]
46	$He_2^+ + N_2 \rightarrow N_2^+ + 2He$	1.1×10^{-15}	0	[81]
47	$N_2^+ + He + N_2 \rightarrow N_4^+ + He$	$8.9 \times 10^{-42}(T_g/300)^{-1.54}$	0	[81]
48	$N_2^+ + N_2 + N_2 \rightarrow N_4^+ + N_2$	5×10^{-41}	0	[82]
49	$He^+ + N_2 + He \rightarrow N_2^+ + 2He$	1.1×10^{-41}	0	[81]
50	$He_2^+ + N_2 + He \rightarrow N_2^+ + 3He$	1.6×10^{-41}	0	[81]
51	$He_m + N_2 + He \rightarrow N_2^+ + 2He + e^-$	3.3×10^{-42}	0	[62]
52	$e^- + O_2 \rightarrow e^- + O_2$	$f(\varepsilon, n)$	0	[78]
53	$e^- + O_2 \rightarrow e^- + O_2 \ (v = 1 \ to \ 4)$	$f(\varepsilon, n)$	0.19, 0.38, 0.6, 0.8	[78]
54	$e^- + O_2 \rightarrow O + O^-$	$f(\varepsilon, n)$	0	[78]
55	$e^- + O_2 \rightarrow e^- + O_2(a)$	$f(\varepsilon, n)$	0.977	[78]
56	$e^- + O_2 \rightarrow e^- + O_2(b)$	$f(\varepsilon, n)$	1.627	[78]
57	$e^- + O_2 \rightarrow e^- + 2O$	$f(\varepsilon, n)$	6	[78]
58	$e^- + O_2 \rightarrow e^- + O + O(^1D)$	$f(\varepsilon, n)$	8.4	[78]
59	$e^- + O_2 \rightarrow e^- + O + O(^1S)$	$f(\varepsilon, n)$	9.97	[78]
60	$e^- + O_2 \rightarrow 2e^- + O_2^+$	$f(\varepsilon, n)$	12.1	[78]
61	$e^- + O_2^+ \rightarrow 2O$	$1.2 \times 10^{-14}T_e^{-0.7}$	0	[83]
62	$e^- + O_2 + O_2 \rightarrow O_2^- + O_2$	$2.26 \times 10^{-42}(T_g/300)^{-0.5}$	0	[84]
63	$e^- + O_2^+ + O_2 \rightarrow 2O_2$	$2.49 \times 10^{-41}(T_e)^{-1.5}$	0	[76]
64	$2e^- + O_2^+ \rightarrow e^- + O_2$	$7.18 \times 10^{-39}(T_e)^{-4.5}$	0	[82]
65	$O_4^+ + O^- + O_2 \rightarrow 2O_2 + O + O_2$	$2 \times 10^{-37}(T_g/300)^{-2.5}$	0	[82,85]
66	$O_4^+ + O_2^- + O_2 \rightarrow 3O_2 + O_2$	$2 \times 10^{-37}(T_g/300)^{-2.5}$	0	[82,85]
67	$O_4^+ + O_2 \rightarrow O_2^+ + 2O_2$	$3.3 \times 10^{-12}(T_g/300)^{-4}e^{(-5030/T_g)}$	0	[82]
68	$e^- + O_4^+ \rightarrow 2O_2$	$2.25 \times 10^{-13}T_e^{-0.5}$	0	[82]
69	$O_4^+ + O^- + He \rightarrow 2O_2 + O + He$	$2 \times 10^{-37}(T_g/300)^{-2.5}$	0	[82,85]
70	$O_4^+ + O_2^- + He \rightarrow 3O_2 + He$	$2 \times 10^{-37}(T_g/300)^{-2.5}$	0	[82,85]
71	$e^- + O_2 + He \rightarrow He + O_2^-$	1×10^{-43}	0	[86]
72	$O_2^+ + O_2 + He \rightarrow O_4^+ + He$	$5.8 \times 10^{-43}(T_g/300)^{-3.1}$	0	[87]
73	$He_m + O_2 \rightarrow O_2^+ + He + e^-$	$2.54 \times 10^{-16}(T_g/300)^{0.5}$	0	[83]
74	$He + He_m + O_2 \rightarrow O_2^+ + 2He + e^-$	1.6×10^{-43}	0	[88]
75	$He_2^m + O_2 \rightarrow O_2^+ + 2He + e^-$	$1 \times 10^{-16}(T_g/300)^{0.5}$	0	[89]
76	$He_2^+ + O_2 \rightarrow O_2^+ + 2He$	$1 \times 10^{-15}(T_g/300)^{0.5}$	0	[89]
77	$O_2^+ + O^- + M \rightarrow O_2 + O + M$	$2 \times 10^{-37}(T_g/300)^{-2.5}$	0	[82,90]
78	$O_2^+ + O_2^- + M \rightarrow 2O_2 + M$	$2 \times 10^{-37}(T_g/300)^{-2.5}$	0	[82,90]
79	$O_2^+ + O^- + M \rightarrow O_3 + M$	$2 \times 10^{-37}(T_g/300)^{-2.5}$	0	[82,90]
80	$O_4^+ + O^- + N_2 \rightarrow 2O_2 + O + N_2$	$1 \times 10^{-37}(T_g/300)^{-2.5}$	0	[82,90]
81	$O_4^+ + O_2^- + N_2 \rightarrow 3O_2 + N_2$	$1 \times 10^{-37}(T_g/300)^{-2.5}$	0	[82,90]
82	$N_2^+ + O^- + M \rightarrow N_2 + O + M$	$2 \times 10^{-37}(T_g/300)^{-2.5}$	0	[82,90]
83	$N_2^+ + O_2^- + M \rightarrow N_2 + O_2 + M$	$2 \times 10^{-37}(T_g/300)^{-2.5}$	0	[82,90]
84	$N_2^+ + O_2 + e^- \rightarrow O_2 + N_2$	$6 \times 10^{-39}(T_e/T_g)^{-1.5}$	0	[90]

85	$O_2^+ + N_2 + e^- \rightarrow O_2 + N_2$	$6 \times 10^{-39}(T_e/T_g)^{-1.5}$	0	[90]
86	$N_4^+ + O_2 \rightarrow O_2 + N_2 + N_2^+$	2.5×10^{-16}	0	[90]
87	$N_2^+ + O_2 \rightarrow N_2 + O_2^+$	$1.04 \times 10^{-15}T_g^{-0.5}$	0	[91]
88	$N_4^+ + O_2 \rightarrow 2N_2 + O_2^+$	2.5×10^{-16}	0	[92]
89	$O_4^+ + N_2 \rightarrow O_2 + N_2 + O_2^+$	$1 \times 10^{-11}(T_g/300)^{-4.2}\exp(-5400/T_g)$	0	[90]
90	$e^- + O_2 + N_2 \rightarrow N_2 + O_2^-$	$1.24 \times 10^{-43}(T_g/300)^{-0.5}$	0	[85]
91	$O_2^+ + O_2 + O_2 \rightarrow O_2 + O_4^+$	$2.4 \times 10^{-32}(T_g/300)^{-3.2}$	0	[82]

a) He_m represents $He(2s^3S)$ and $He(2s^1S)$; He_2^m represents $He_2(a^3\Sigma_u^+)$; $O_2(a)$ represents $O_2(a^1\Delta_g)$ and are treated as O_2; $O_2(b)$ represents $O_2(b^1\Sigma_g^+)$ and are treated as O_2; $N_2(v)$ represents the vibrational excited states of $N_2(v = 1 - 4)$ and are treated as N_2; $N_2(A^3\Sigma_u^+ (v = 0 - 4))$, $N_2(A^3\Sigma_u^+ (v = 5 - 9))$, $N_2(A^3\Sigma_u^+ (v > 9))$, $N_2(B^3\Pi_g)$, $N_2(W^3\Delta_u)$, $N_2(B^3\Sigma_u^-)$, $N_2(a^1\Sigma_u^-)$, $N_2(a^1\Pi_g)$, $N_2(W^1\Delta_u)$, $N_2(C^3\Pi_u)$, $N_2(E^3\Sigma_g^+)$, $N_2(a^1\Sigma_g^+)$ are treated as N_2; $O_2(v)$ represents the vibrational excited states of $O_2(v = 1 - 4)$ and are treated as O_2; $O(^1D)$ and $O(^1S)$ are treated as O. M represents the background gases helium atom, nitrogen and oxygen molecule. b) Rate coefficients have units of $s^{-1}, m^3s^{-1}, m^6s^{-1}$ for one, two and three body reactions respectively; $T_e = 2/3\varepsilon$ has units eV; T_g has units of K. $f(\varepsilon, n)$ indicates the rate coefficient as a function of the mean electron energy and air mole fraction calculated from the solution of Boltzmann equation. The reference indicates the database of the cross section used.
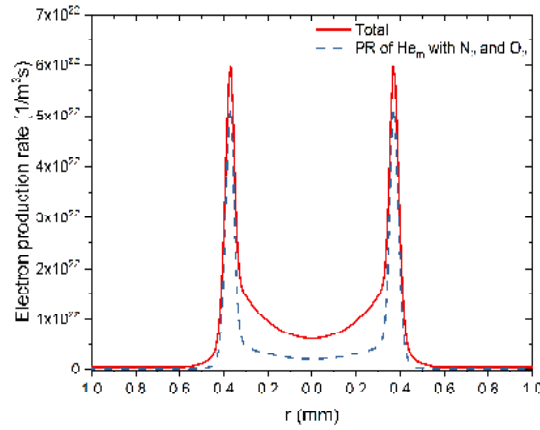
Appendix B.

Figure 19: Simulation results of the electron production rate for the He plasma jet at z=0.1 mm and time -152 ns (i.e. streamer head location at z=-0.75 mm, same time snapshot as Figure 6a).
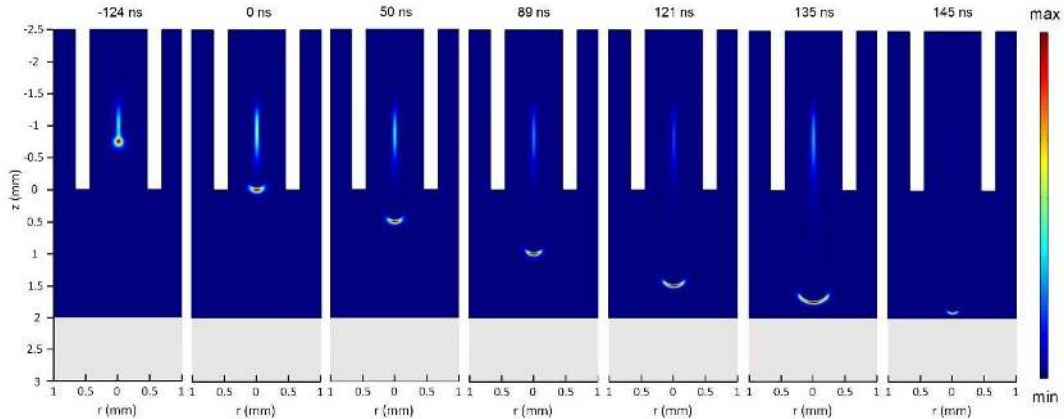

Figure 20: Simulation results of the spatio-temporal evolution of the total ionization rate for He plasma jet without considering the Penning reactions in the kinetic scheme.
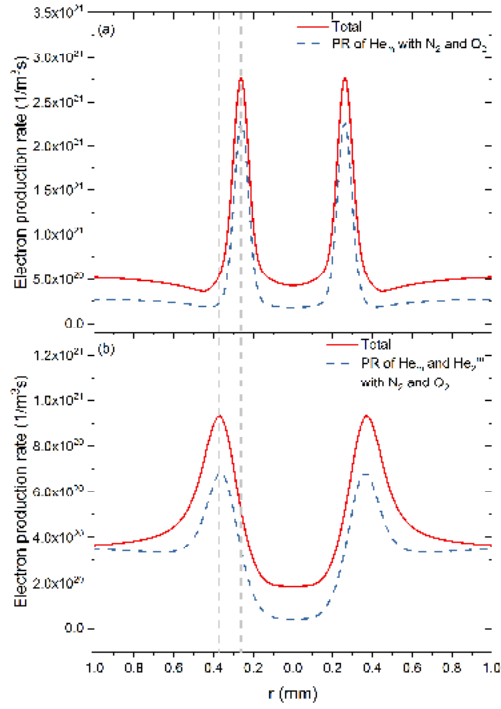
Figure 21: Simulation results of the electron production rate for the He plasma jet (a) at z=1 mm and time 0 ns (i.e. streamer head location at z=0 mm, same time snapshot as Figure 6c), (b) at z=1.85 and time 121 ns (i.e. streamer head location at z=1 mm, same time snapshot as Figure 6e). The dotted grey lines are a visual aid to highlight the peak shift between the two curves.
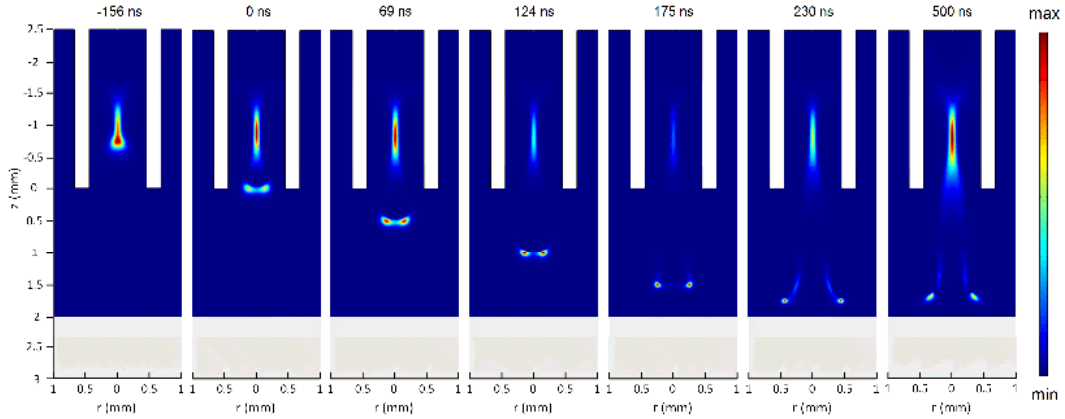

Figure 22: Simulation results of the spatio-temporal evolution of the total ionization rate for He plasma jet where the seec is set to zero.
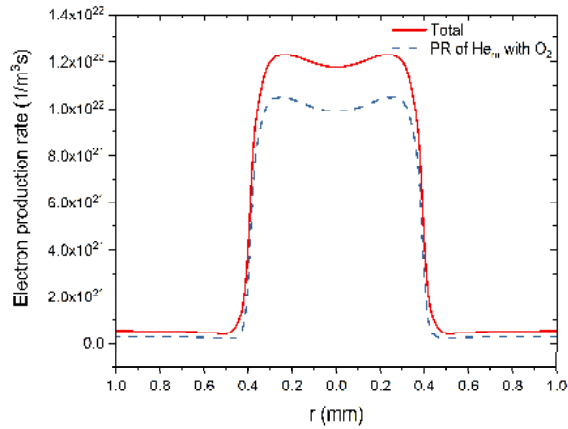
Figure 23: Simulation results of the electron production rate for the He+O$_2$ (1000ppm) plasma jet at z=0.1 mm and time -181 ns (i.e. plasma bullet location z= -0.75 mm, same time snapshot as Figure 12a).
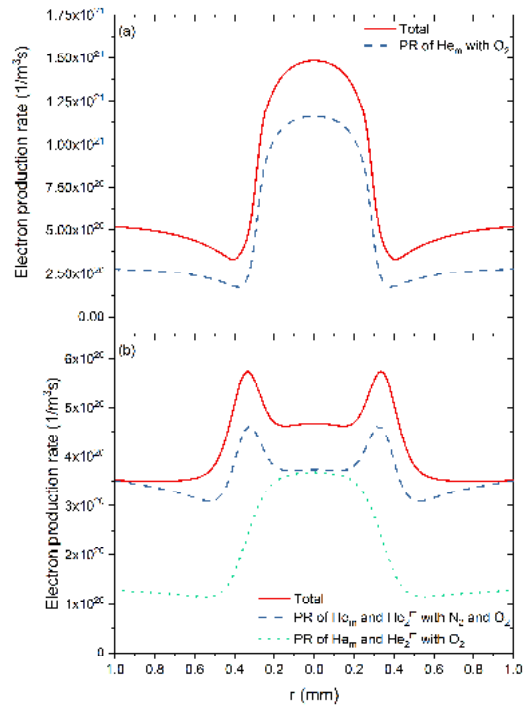

Figure 24: Simulation results of the electron production rate for the He+O$_2$ (1000 ppm) plasma jet (a) at z=1 mm and time 0 ns (i.e. the plasma bullet location just about the exit of the tube, same time snapshot as Figure 12c), (b) at z=1.85 and time 163 ns (i.e. plasma bullet location z= 1 mm, same time snapshot as Figure 12e).
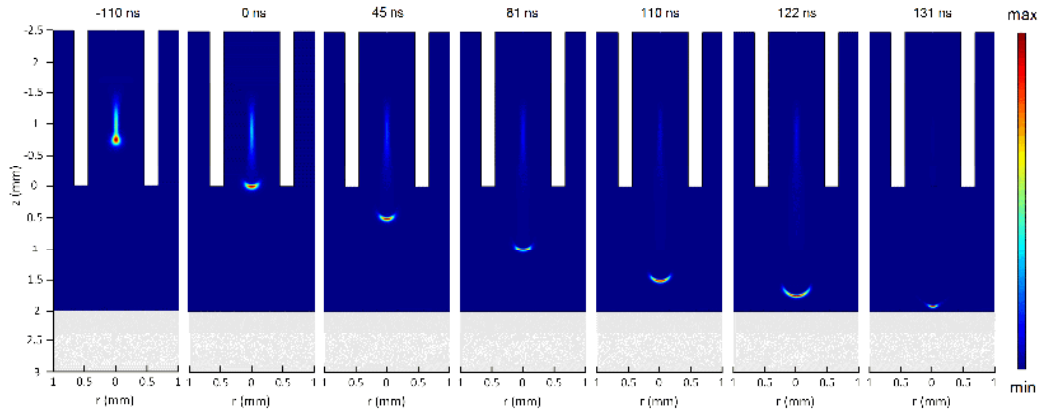
Figure 25: Simulation results of the spatio-temporal evolution of the total ionization rate for He+O_2 (1000 ppm) plasma jet without considering the Penning reactions in the kinetic scheme.
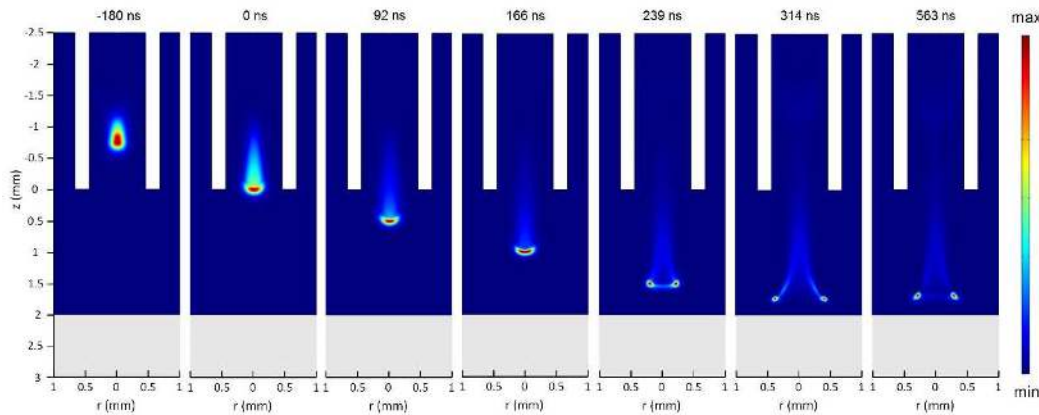

Figure 26: Simulation results of the spatio-temporal evolution of the total ionization rate for He+O_2 (1000 ppm) plasma jet where the seec is set to zero.

References:

[1]   Svarnas P, Asimakoulas L, Katsafadou M, Pachis K, Kostazos N and Antimisiaris S G 2017 Liposomal membrane disruption by means of miniaturized dielectric-barrier discharge in air: liposome characterization *J. Phys. D. Appl. Phys.* **50** 345403

[2]   Topala I and Nagatsu M 2015 Capillary plasma jet: A low volume plasma source for life science applications *Appl. Phys. Lett.* **106** 054105

[3]   Barwe B, Stein A, Cibulka O E, Pelant I, Ghanbaja J, Belmonte T and Benedikt J 2015 Generation of Silicon Nanostructures by Atmospheric Microplasma Jet: The Role of Hydrogen Admixture *Plasma Process. Polym.* **12** 132–40

[4]   Vandamme M, Robert E, Lerondel S, Sarron V, Ries D, Dozias S, Sobilo J, Gosset D, Kieda C, Legrain B, Pouvesle J-M and Pape A Le 2012 ROS implication in a new antitumor strategy based on non-thermal plasma *Int. J. Cancer* **130** 2185–94

[5]   Laroussi M 2015 Low-Temperature Plasma Jet for Biomedical Applications: A Review *IEEE Trans. Plasma Sci.* **43** 703–12

[6]   Graves D B 2014 Low temperature plasma biomedicine: A tutorial review *Phys. Plasmas* **21**

[7]   Fridman G, Friedman G, Gutsol A, Shekhter A B, Vasilets V N and Fridman A 2008 Applied Plasma Medicine *Plasma Process. Polym.* **5** 503–33

[8]   Adamovich I, Baalrud S D, Bogaerts A, Bruggeman P J, Cappelli M, Colombo V, Czarnetzki U, Ebert U, Eden J G, Favia P, Graves D B, Hamaguchi S, Hieftje G, Hori M, Kaganovich I D, Kortshagen U, Kushner M J, Mason N J, Mazouffre S, Thagard S

M, Metelmann H-R, Mizuno A, Moreau E, Murphy A B, Niemira B A, Oehrlein G S, Petrovic Z L, Pitchford L C, Pu Y-K, Rauf S, Sakai O, Samukawa S, Starikovskaia S, Tennyson J, Terashima K, Turner M M, van de Sanden M C M and Vardelle A 2017 The 2017 Plasma Roadmap: Low temperature plasma science and technology *J. Phys. D. Appl. Phys.* **50** 323001

[9]   Kim S J, Chung T H, Bae S H and Leem S H 2010 Induction of apoptosis in human breast cancer cells by a pulsed atmospheric pressure plasma jet *Appl. Phys. Lett.* **97** 023702

[10]   Mirpour S, Ghomi H, Piroozmand S, Nikkhah M, Tavassoli S H and Azad S Z 2014 The Selective Characterization of Nonthermal Atmospheric Pressure Plasma Jet on Treatment of Human Breast Cancer and Normal Cells *IEEE Trans. Plasma Sci.* **42** 315–22

[11]   Teschke M, Kedzierski J, Finantu-Dinu E G, Korzec D and Engemann J 2005 High-speed photographs of a dielectric barrier atmospheric pressure plasma jet *IEEE Trans. Plasma Sci.* **33** 310–1

[12]   Lu X and Laroussi M 2006 Dynamics of an atmospheric pressure plasma plume generated by submicrosecond voltage pulses *J. Appl. Phys.* **100** 063302

[13]   Lu X, Laroussi M and Puech V 2012 On atmospheric-pressure non-equilibrium plasma jets and plasma bullets *Plasma Sources Sci. Technol.* **21** 034005

[14]   Lu X, Naidis G V, Laroussi M and Ostrikov K 2014 Guided ionization waves: Theory and experiments *Phys. Rep.* **540** 123–66

[15]   Wu S, QuanJun Huang, Zhan Wang and XinPei Lu 2011 The Effect of Nitrogen Diffusion From Surrounding Air on Plasma Bullet Behavior *IEEE Trans. Plasma Sci.* **39** 2286–7

[16]   Leiweke R J, Sands B L and Ganguly B N 2011 Effect of Gas Mixture on Plasma Jet Discharge Morphology *IEEE Trans. Plasma Sci.* **39** 2304–5

[17]   Chang Z, Yao C, Mu H and Zhang G 2014 Study on the Property Evolution of Atmospheric Pressure Plasma Jets in Helium *Plasma Sci. Technol.* **16** 83–8

[18]   Xian Y, Yue Y, Liu D, Yang Y, Lu X and Pan Y 2014 On the Mechanism of Ring-Shape Structure of Plasma Bullet *Plasma Process. Polym.* **11** 1169–74

[19]   Karakas E, Koklu M and Laroussi M 2010 Correlation between helium mole fraction and plasma bullet propagation in low temperature plasma jets *J. Phys. D. Appl. Phys.* **43** 155202

[20]   Robert E, Sarron V, Riès D, Dozias S, Vandamme M and Pouvesle J-M 2012 Characterization of pulsed atmospheric-pressure plasma streams (PAPS) generated by a plasma gun *Plasma Sources Sci. Technol.* **21** 034017

[21]   Darny T, Pouvesle J-M, Puech V, Douat C, Dozias S and Robert E 2017 Analysis of conductive target influence in plasma jet experiments through helium metastable and electric field measurements *Plasma Sources Sci. Technol.* **26** 045008

[22]   Robert E, Darny T, Dozias S, Iseni S and Pouvesle J M 2015 New insights on the propagation of pulsed atmospheric plasma streams: From single jet to multi jet arrays *Phys. Plasmas* **22** 122007

[23]   van der Schans M, Böhm P, Teunissen J, Nijdam S, IJzerman W and Czarnetzki U 2017 Electric field measurements on plasma bullets in N 2 using four-wave mixing *Plasma Sources Sci. Technol.* **26** 115006

[24]   Viegas P, Péchereau F and Bourdon A 2018 Numerical study on the time evolutions of the electric field in helium plasma jets with positive and negative polarities *Plasma Sources Sci. Technol.* **27** 025007

[25]   Pechereau F, Bonaventura Z and Bourdon A 2016 Influence of surface emission processes on a fast-pulsed dielectric barrier discharge in air at atmospheric pressure *Plasma Sources Sci. Technol.* **25** 044004

[26]   Busco G, Fasani F, Dozias S, Ridou L, Douat C, Pouvesle J-M, Robert E and Grillon C 2017 CHANGES IN OXYGEN LEVEL UPON COLD PLASMA TREATMENTS: CONSEQUENCES FOR RONS PRODUCTION *IEEE Trans. Radiat. Plasma Med. Sci.* 1–1

[27]   Gazeli K, Svarnas P, Held B, Marlin L and Clément F 2015 Possibility of controlling the chemical pattern of He and Ar "guided streamers" by means of N 2 or O 2 additives *J. Appl. Phys.* **117** 093302

[28]   Klute F D, Michels A, Schütz A, Vadla C, Horvatic V and Franzke J 2016 Capillary Dielectric Barrier Discharge: Transition from Soft Ionization to Dissociative Plasma *Anal. Chem.* **88** 4701–5

[29]   Klute F D, Schütz A, Michels A, Vadla C, Veza D, Horvatic V and Franzke J 2016 An experimental study on the influence of trace impurities on ionization of atmospheric noble gas dielectric barrier discharges *Analyst* **141** 5842–8

[30]   Douat C, Kacem I, Sadeghi N, Bauville G, Fleury M and Puech V 2016 Space-time resolved density of helium metastable atoms in a nanosecond pulsed plasma jet: influence of high voltage and pulse frequency *J. Phys. D. Appl. Phys.* **49** 285204

[31]   Douat C, Hübner S, Engeln R and Benedikt J 2016 Production of nitric/nitrous oxide by an atmospheric pressure plasma jet *Plasma Sources Sci. Technol.* **25** 025027

[32]   Naidis G V 2010 Modelling of streamer propagation in atmospheric-pressure helium plasma jets *J. Phys. D. Appl. Phys.* **43** 402001

[33]   Naidis G V 2011 Modelling of plasma bullet propagation along a helium jet in ambient air *J. Phys. D. Appl. Phys.* **44** 215203

[34]   Breden D, Miki K and Raja L L 2011 Computational study of cold atmospheric nanosecond pulsed helium plasma jet in air *Appl. Phys. Lett.* **99** 111501

[35]   Jánský J and Bourdon A 2011 Simulation of helium discharge ignition and dynamics in thin tubes at atmospheric pressure *Appl. Phys. Lett.* **99** 161504

[36]   Breden D, Miki K and Raja L L 2012 Self-consistent two-dimensional modeling of cold atmospheric-pressure plasma jets/bullets *Plasma Sources Sci. Technol.* **21** 034011

[37]   Naidis G V. 2012 Modeling of helium plasma jets emerged into ambient air: Influence of applied voltage, jet radius, and helium flow velocity on plasma jet characteristics *J. Appl. Phys.* **112** 103304

[38]   Boeuf J-P, Yang L L and Pitchford L C 2013 Dynamics of a guided streamer ("plasma bullet") in a helium jet in air at atmospheric pressure *J. Phys. D. Appl. Phys.* **46** 015201

[39]   Liu X Y, Pei X K, Lu X P and Liu D W 2014 Numerical and experimental study on a pulsed-dc plasma jet *Plasma Sources Sci. Technol.* **23** 035007

[40]   Naidis G V. 2015 On the Ring-Shaped Structure of Helium Plasma Jets *IEEE Trans. Plasma Sci.* **43** 733–6

[41]   Bourdon A, Darny T, Pechereau F, Pouvesle J-M, Viegas P, Iséni S and Robert E 2016 Numerical and experimental study of the dynamics of a µ s helium plasma gun discharge with various amounts of N 2 admixture *Plasma Sources Sci. Technol.* **25** 035002

[42]   Norberg S A, Johnsen E and Kushner M J 2015 Formation of reactive oxygen and nitrogen species by repetitive negatively pulsed helium atmospheric pressure plasma jets propagating into humid air *Plasma Sources Sci. Technol.* **24** 035026

[43]   Logothetis D, Papadopoulos P K, Svarnas P and Vafeas P 2016 Comparison of two electro-hydrodynamic force models for the interaction between helium jet flow and an atmospheric-pressure "plasma jet" p 150019

[44]   Lietz A M, Johnsen E and Kushner M J 2017 Plasma-induced flow instabilities in atmospheric pressure plasma jets *Appl. Phys. Lett.* **111** 114101

[45]   Ning W, Dai D, Zhang Y, Han Y and Li L 2018 Effects of trace of nitrogen on the helium atmospheric pressure plasma jet interacting with a dielectric substrate *J. Phys. D. Appl. Phys.* **51** 125204

[46]   Norberg S A, Johnsen E and Kushner M J 2015 Helium atmospheric pressure plasma jets touching dielectric and metal surfaces *J. Appl. Phys.* **118** 013301

[47]   Norberg S A, Johnsen E and Kushner M J 2016 Helium atmospheric pressure plasma jets interacting with wet cells: delivery of electric fields *J. Phys. D. Appl. Phys.* **49** 185201

[48]   Wang L, Zheng Y and Jia S 2016 Numerical study of the interaction of a helium

atmospheric pressure plasma jet with a dielectric material *Phys. Plasmas* **23** 103504

[49]　Yan W and Economou D J 2016 Simulation of a non-equilibrium helium plasma bullet emerging into oxygen at high pressure (250–760 Torr) and interacting with a substrate *J. Appl. Phys.* **120** 123304

[50]　Yan W and Economou D J 2017 Gas flow rate dependence of the discharge characteristics of a helium atmospheric pressure plasma jet interacting with a substrate *J. Phys. D. Appl. Phys.* **50** 415205

[51]　Brandt S, Klute F D, Schütz A and Franzke J 2017 Dielectric barrier discharges applied for soft ionization and their mechanism *Anal. Chim. Acta* **951** 16–31

[52]　Logothetis D K, Papadopoulos P K, Svarnas P and Vafeas P 2016 Numerical simulation of the interaction between helium jet flow and an atmospheric-pressure "plasma jet" *Comput. Fluids* **140** 11–8

[53]　Lazarou C, Belmonte T, Chiper A S and Georghiou G E 2016 Numerical modelling of the effect of dry air traces in a helium parallel plate dielectric barrier discharge *Plasma Sources Sci. Technol.* **25**

[54]　Russell T W F, Robinson A S and Wagner N J Convective Heat and Mass Transfer *Mass and Heat Transfer* (Cambridge: Cambridge University Press) pp 246–300

[55]　Papadopoulos P K, Vafeas P, Svarnas P, Gazeli K, Hatzikonstantinou P M, Gkelios A and Clément F 2014 Interpretation of the gas flow field modification induced by guided streamer ("plasma bullet") propagation *J. Phys. D. Appl. Phys.* **47** 425203

[56]　Wilke C R 1950 A Viscosity Equation for Gas Mixtures *J. Chem. Phys.* **18** 517–9

[57]　Day M A 1990 The no-slip condition of fluid dynamics *Erkenntnis* **33** 285–96

[58]　Anon COMSOL Multiphysics® v. 4.4. www.comsol.com. COMSOL AB, Stockholm, Sweden.

[59]　Hagelaar G J M and Pitchford L C 2005 Solving the Boltzmann equation to obtain electron transport coefficients and rate coefficients for fluid models *Plasma Sources Sci. Technol.* **14** 722–33

[60]　Tschiersch R, Nemschokmichal S, Bogaczyk M and Meichsner J 2017 Surface charge measurements on different dielectrics in diffuse and filamentary barrier discharges *J. Phys. D. Appl. Phys.* **50** 105207

[61]　Shashurin A and Keidar M 2015 Experimental approaches for studying non-equilibrium atmospheric plasma jets *Phys. Plasmas* **22** 122002

[62]　Pouvesle J M 1982 Modeling of the charge transfer afterglow excited by intense electrical discharges in high pressure helium nitrogen mixtures *J. Chem. Phys.* **77** 817

[63]　Sakiyama Y, Graves D B, Jarrige J and Laroussi M 2010 Finite element analysis of ring-shaped emission profile in plasma bullet *Appl. Phys. Lett.* **96** 041501

[64]　Belinger A, Naudé N and Gherardi N 2017 Transition from diffuse to self-organized discharge in a high frequency dielectric barrier discharge ed N Gherardi and T Hoder *Eur. Phys. J. Appl. Phys.* **79** 10802

[65]　Schregel C-G, Carbone E A D, Luggenhölscher D and Czarnetzki U 2016 Ignition and afterglow dynamics of a high pressure nanosecond pulsed helium micro-discharge: I. Electron, Rydberg molecules and He (2 3 S) densities *Plasma Sources Sci. Technol.* **25** 054003

[66]　Carbone E A D, Schregel C-G and Czarnetzki U 2016 Ignition and afterglow dynamics of a high pressure nanosecond pulsed helium micro-discharge: II. Rydberg molecules kinetics *Plasma Sources Sci. Technol.* **25** 054004

[67]　Nemschokmichal S, Tschiersch R and Meichsner J 2016 The influence of negative ions in helium–oxygen barrier discharges: II. 1D fluid simulation and adaption to the experiment *Plasma Sources Sci. Technol.* **25** 055024

[68]　Martens T, Bogaerts A, Brok W J M and van Dijk J 2010 The influence of impurities on the performance of the dielectric barrier discharge *Appl. Phys. Lett.* **96** 091501

[69]　Yan W, Liu F, Sang C and Wang D 2014 Two-dimensional modeling of the cathode sheath formation during the streamer-cathode interaction *Phys. Plasmas* **21** 013504

[70]　Anon Morgan database, www.lxcat.net, retrieved on September 25, 2015

[71]　Lieberman M a 2015 Analytical model of atmospheric pressure, helium/trace gas

radio-frequency capacitive Penning discharges *Plasma Sources Sci. Technol.* **24** 025009

[72] Deloche R, Monchicourt P, Cheret M and Lambert F 1976 High-pressure helium afterglow at room temperature *Phys. Rev. A* **13** 1140–76

[73] Stevefelt J 1982 Reaction kinetics of a high pressure helium fast discharge afterglow *J. Chem. Phys.* **76** 4006

[74] Konstantinovskii R S, Shibkov V M and Shibkova L V 2005 Effect of a Gas Discharge on the Ignition in the Hydrogen – Oxygen System **46** 821–34

[75] Wang Q, Economou D J and Donnelly V M 2006 Simulation of a direct current microplasma discharge in helium at atmospheric pressure *J. Appl. Phys.* **100** 023301

[76] Gordillo-Vázquez F J 2008 Air plasma kinetics under the influence of sprites *J. Phys. D. Appl. Phys.* **41** 234016

[77] Golubovskii Y B, Maiorov V A, Behnke J and Behnke J F 2003 Modelling of the homogeneous barrier discharge in helium at atmospheric pressure *J. Phys. D. Appl. Phys.* **36** 39–49

[78] Anon IST-Lisbon database, www.lxcat.net, retrieved on September 25, 2015

[79] Sommerer T J and Kushner M J 1992 Numerical investigation of the kinetics and chemistry of rf glow discharge plasmas sustained in He, N2, O2, He/N2/O2, He/CF4/O2, and SiH4/NH3 using a Monte Carlo-fluid hybrid model *J. Appl. Phys.* **71** 1654

[80] Raja L L 2003 Computational study of capacitively coupled high-pressure glow discharges in helium *IEEE Trans. Plasma Sci.* **31** 495–503

[81] Margot J, Petrov G M, Matte J P, Pe I, Sadi T, Hubert J, Tran K C, Alves L L, Loureiro J, Ferreira C M and Guerra V 2000 Numerical Modeling of a He – N 2 Capillary Surface ´re **20**

[82] Kossyi I A, Kostinsky A Y, Matveyev A A and Silakov V P 1992 Kinetic scheme of the non-equilibrium discharge in nitrogen-oxygen mixtures *Plasma Sources Sci. Technol.* **1** 207–20

[83] Stafford D S and Kushner M J 2004 O[sub 2]([sup 1]Δ) production in He∕O[sub 2] mixtures in flowing low pressure plasmas *J. Appl. Phys.* **96** 2451

[84] Park G Y, Hong Y J, Lee H W, Sim J Y and Lee J K 2010 A Global Model for the Identification of the Dominant Reactions for Atomic Oxygen in He/O 2 Atmospheric-Pressure Plasmas *Plasma Process. Polym.* **7** 281–7

[85] Liu D-X, Rong M-Z, Wang X-H, Iza F, Kong M G and Bruggeman P 2010 Main Species and Physicochemical Processes in Cold Atmospheric-pressure He + O2 Plasmas *Plasma Process. Polym.* **7** 846–65

[86] Stalder K R, Vidmar R J, Nersisyan G and Graham W G 2006 Modeling the chemical kinetics of high-pressure glow discharges in mixtures of helium with real air *J. Appl. Phys.* **99** 093301

[87] Good A 1975 Third-order ion-molecule clustering reactions *Chem. Rev.* **75** 561–83

[88] Niemi K, Waskoenig J, Sadeghi N, Gans T and O'Connell D 2011 The role of helium metastable states in radio-frequency driven helium–oxygen atmospheric pressure plasma jets: measurement and numerical simulation *Plasma Sources Sci. Technol.* **20** 055005

[89] Cardoso R P, Belmonte T, Henrion G and Sadeghi N 2006 Influence of trace oxygen on He(2 3 S) density in a He–O 2 microwave discharge at atmospheric pressure: behaviour of the time afterglow *J. Phys. D. Appl. Phys.* **39** 4178–85

[90] Murakami T, Niemi K, Gans T, O'Connell D and Graham W G 2013 Chemical kinetics and reactive species in atmospheric pressure helium–oxygen plasmas with humid-air impurities *Plasma Sources Sci. Technol.* **22** 015003

[91] Kelly S and Turner M M 2013 Atomic oxygen patterning from a biomedical needle-plasma source *J. Appl. Phys.* **114** 123301

[92] Brandenburg R, Maiorov V A, Golubovskii Y B, Wagner H-E, Behnke J and Behnke J F 2005 Diffuse barrier discharges in nitrogen with small admixtures of oxygen: discharge mechanism and transition to the filamentary regime *J. Phys. D. Appl. Phys.*

38 2187–97